The cortical microtubules of *Toxoplasma gondii* underlie the helicity of parasite movement

Isadonna F. Tengganu[1#], Luisa F. Arias Padilla[1#], Jonathan Munera Lopez[1#], Jun Liu[2,3], Peter T. Brown[4], John M. Murray[1], Ke Hu[1*]

[1]Biodesign Center for Mechanisms of Evolution/School of Life Sciences, Arizona State University, USA
[2]Department of Biology, Indiana University, USA
[3]Current address: Berkgen Biopharmaceuticals, Shenzhen, China
[4]Department of Physics and Center for Biological Physics, Arizona State University, USA

#: equal contribution

**: Address correspondence to:*
Email: kehu4@asu.edu

Running title: *cortical microtubules facilitate helical parasite movement*

ABSTRACT

Motility is essential for apicomplexan parasites to infect their hosts. In a three-dimensional (3-D) environment, the apicomplexan parasite *Toxoplasma gondii* moves along a helical path. The cortical microtubules, which are ultra-stable and spirally arranged, have been considered to be a structure that guides the long-distance movement of the parasite. Here we address the role of the cortical microtubules in parasite motility, invasion, and egress by utilizing a previously generated mutant (dubbed "TKO") in which these microtubules are destabilized in mature parasites. We found that the cortical microtubules in ~ 80% of the non-dividing (i.e. daughter-free) TKO parasites are much shorter than normal. The extent of depolymerization is further exacerbated upon commencement of daughter formation or cold treatment, but parasite replication is not affected. In a 3-D Matrigel matrix, the TKO mutant moves directionally over long distances, but along trajectories significantly more linear (i.e. less helical) than those of wild-type parasites. Interestingly, this change in trajectory does not impact either movement speed in the matrix or the speed and behavior of the parasite's entry into and egress from the host cell.

INTRODUCTION

Apicomplexans are obligate intracellular parasites, many of which are important pathogens. For example, the malaria parasites, *Plasmodium* spp., kill more than half a million people each year (World-Health-Organization, 2022). *Toxoplasma gondii* permanently infects ~ 20% of the global human population and can infect any warm-blooded animal (Dubey, 2008). As obligate intracellular organisms, a successful infection requires the parasite to travel over a long distance through tissues with varying biochemical and biophysical properties (Hopp et al., 2015) as well as to enter into host cells. The latter requires a shorter travel distance, but perhaps more finesse, as the host cell plasma membrane needs to remain intact to allow the parasite to use host cell resources for proliferation.

Toxoplasma gondii moves along an irregular helical path in tissues and in a three-dimensional (3-D) matrix over tens of microns (Leung et al., 2014). Chemical inhibition as well as genetic manipulations showed that actin and a series of apical and cortical myosin motors provide the underlying force for the parasite motility (Dobrowolski et al., 1997; Gaskins et al., 2004; Graindorge et al., 2016; Heaslip et al., 2011; Meissner et al., 2002). The current model posits that the internal force is transmitted to the parasite surface through a coupling between the actomyosin complex and the secreted transmembrane adhesins (Opitz and Soldati, 2002). The characterization of these factors has significantly advanced the understanding of parasite motility (Dobrowolski et al., 1997; Frenal et al., 2010; Gaskins et al., 2004; Graindorge et al., 2016; Heaslip et al., 2011; Huynh and Carruthers, 2006; Huynh et al., 2003; Jacot et al., 2016; Meissner et al., 2002; Tosetti et al., 2019). However, while actin polymerization is critical for parasite movement, no native actin filaments have been detected, suggesting that the polymerization is likely to occur dynamically (Dobrowolski and Sibley, 1996; Mehta and Sibley, 2011; Periz et al., 2017; Sahoo et al., 2006; Schatten et al., 2003; Wetzel et al., 2003). Thus, it is still not known how the parasite is capable of traveling over long distances along a helical path. Intuitively, a stable, inherently helical cortical structure would be required for guiding continuous parasite movement over a long distance.

In *Toxoplasma,* one of the main cytoskeletal structures with a roughly helical arrangement is the set of cortex-associating (denoted as "subpellicular" or "cortical") microtubules that are anchored at one end in a ring-like structure (the apical polar ring) at the parasite apex (Leung et al., 2017; Morrissette and Sibley, 2002a; Nichols and Chiappino, 1987). Among the apicomplexans, the microtubule cytoskeleton displays intriguing species and life-stage specific variations that coincide with substantial differences in physiology. The mature *Plasmodium* ookinete has an intricate cage of ~ 60 cortical microtubules (Bounkeua et al., 2010; Garnham et al., 1962; Wang et al., 2020), but the asexual blood-stage parasites only have a narrow band of 2-4 cortical microtubules that extends down one side of the parasite (Bannister and Mitchell, 1995; Morrissette and Sibley, 2002a). The *Toxoplasma* tachyzoite has consistently 22 cortical microtubules that are arranged in a spiral pattern. The parasite invests a considerable amount of resources in building and maintaining these polymers. Aside from the core building blocks, the tubulins, there is a suite of proteins that associate with the cortical microtubules in a region-specific manner (Leung et al., 2017; Liu et al., 2015; Liu et al., 2013; Tran et al., 2012). In mature parasites, these microtubules form an ultra-stable "rib cage" that extensively interacts with the inner membrane complex (IMC). They remain intact under treatments that depolymerize microtubules in mammalian cells within minutes (Hu et al., 2002; Morrissette et al., 1997). This extraordinary stability makes it difficult to assess the function of these polymers in the mature parasite.

Previously, a suite of proteins have been found to associate with the cortical microtubules. Some of them do not bind along the entire length of the microtubule, but are restricted to distinct regions (Liu et al., 2015; Liu et al., 2013; Tran et al., 2012). We discovered that, in mature parasites, TLAP2 and SPM1 together stabilize the portion of the microtubules distal to the apical section, which contains TLAP3 (Liu et al., 2015). In the absence of TLAP2 and SPM1, TLAP3 stabilizes the apical section of the cortical microtubules (Liu et al., 2015). Thus in the mutant that lacks TLAP2, SPM1 and TLAP3 (*Δtlap2Δspm1Δtlap3,* denoted "TKO" for succinctness) the stability of the cortical microtubules in mature parasites is dramatically reduced. In the present work, we quantified the proportion of parasites with various levels of defects in the microtubule array under different conditions and found that ~ 80% of the TKO parasites that are not forming daughters (i.e. "non-dividing" in our terminology) have severely curtailed cortical microtubules. Depolymerization in mature TKO parasites becomes even more pronounced upon the initiation of daughter construction or cold treatment, the latter effect being partly reversible. While microtubule polymerization is essential for generating viable daughter cells, parasite replication is not affected by the destabilization of the cortical microtubules in the mature parasite. In a 3-D Matrigel matrix, the TKO mutant parasite moves as persistently as the wild-type parasite with similar velocity and net displacement. However, it travels along a path significantly more linear than the wild-type parasite. Interestingly, even though the cytolytic efficiency of the TKO parasite is significantly lower, live cell imaging revealed that the parasite's behaviors during entry into and egress from the host cell are indistinguishable from those of the wild-type. This indicates that host cell entry and egress, which involve short-distance travel, is less sensitive to structural changes in the parasite than overall infection efficiency.

RESULTS

In TKO parasites, the daughter microtubule array is intact and replication proceeds normally

Previously, we showed qualitatively that the cortical microtubules in mature TKO parasites are destabilized compared with those in the wild-type parasites (Liu et al., 2015). Here, to quantify the extent of destabilization, we determined the proportions of TKO and wild-type parental (RH*Δhx, (Donald and Roos, 1994)*) parasites that display various characteristics in the microtubule array. We first examined wild-type and TKO parasites that do not contain visible daughters based on anti-tubulin labeling (denoted as "non-dividing" in what follows). We found that while 100% of the wild-type parasites have a full, regularly arranged array, the cortical microtubules are severely curtailed in 79% (±8.5% STDEV) of TKO parasites ("short" phenotype) and sparse in the rest (Fig 1A) (Three independent experiments, total 490 parasites analyzed for the TKO and 246 parasites analyzed for the wild-type). The “short” and "sparse" phenotypes are defined as follows: "short"- microtubules at approximately normal density extend to less than 1/3 of the parasite body length and very few microtubules are longer than ~ 1/2 of the parasite body length. "sparse"- more microtubules are longer than 1/2 of the parasite body length but there are obvious gaps in the array. The extent of depolymerization in mature TKO parasites is more pronounced during cell division (Fig 1B-C). The proportion of parasites with nearly fully depolymerized cortical microtubules ("absent" category) was ~ 42% at the initiation stage of daughter construction and increased to ~ 98% prior to daughter emergence from the mother parasite (Fig 1C). For wild-type parasites, the cortical microtubules of the mother parasite in the initiation and elongation stages of daughter construction are similar to that of the non-dividing stage (Fig 1B-C). However, ~ 24% of mature parasites at the pre-emergence stage and 100% during daughter emergence have short

144 microtubules.
145
146 We examined the average number of rounds of replication at 12, 24, and 36 hours after
147 infection and found that the rate of replication of the TKO parasite is very similar to that of the
148 wild-type parasite (Fig 1D). At first glance, it is surprising that a mutant that has destabilized
149 cortical microtubules does not have a replication defect, because microtubule polymerization is
150 coupled with cortex formation, and thus is required for daughter growth (Hu, 2008; Hu et al.,
151 2006; Morrissette and Sibley, 2002b; Stokkermans et al., 1996). However, as we observed
152 previously (Liu et al., 2015), in the same cell in which the cortical microtubules of the mother
153 TKO parasite are depolymerized, microtubules do polymerize in growing daughters, which
154 develop normally. These results reveal a cell-stage dependent microtubule depolymerizing
155 activity that acts on the cortical microtubules in mature parasites but not the polymerizing
156 microtubules in growing daughters. The depolymerization of cortical microtubules in mature
157 TKO parasites becomes apparent at a much earlier stage of daughter formation and is much
158 more complete than in the wild-type parasites, likely because the former are already
159 destabilized due to the lack of TLAP2, TLAP3, and SPM1.
160
161 In our previous work, we showed that incubation at ~ 8°C can further destabilize the
162 cortical microtubules of the TKO parasite (Liu et al., 2015). Here we characterize the time
163 course of cold-induced disassembly of cortical MTs in mature TKO parasites and found that,
164 as expected, the extent of depolymerization increased with the time of cold-treatment (Fig 1E).
165 After ~ 2 hr of cold-treatment (C120), cortical MTs in ~ 72% of the parasites are nearly
166 completely depolymerized with no visible MTs ("absent" category) and only a small tubulin-
167 positive "cap" at the apical end. On the other hand, the array of cortical microtubules in wild-
168 type parasites is not affected by the cold treatment. The cold-induced depolymerization in the
169 TKO parasites is partially reversible (Fig 1E). When TKO cultures cold-treated for 2 hr were
170 returned to 37°C, the cortical MTs were restored significantly after 20 min of the temperature
171 shift. Upon 1hr of 37°C incubation (R60), ~ 80% of the parasites showed patterns ("short or
172 sparse") similar to those of untreated parasites, with the microtubules concentrated at the
173 apical end of the parasite (Fig 1E), suggesting a strong preference for regrowth from pre-
174 existing nucleation sites.
175
176 The preceding experiments were carried out with intracellular parasites residing in host
177 cells. As the difference between intra and extracellular environment may affect subcellular
178 structures in the parasite, we next examined the microtubule array in extracellular wild-type
179 parental (RH*Δhx*) and TKO (*Δtlap2Δspm1Δtlap3*) parasites. We found that the distribution of
180 different array morphologies was similar to what was observed in intracellular mature parasites
181 (Fig 2A&B). More than 94% of the parental parasites have a full, regularly arranged array with
182 and without cold-treatment. In contrast, the cortical microtubules are short in ~ 69% (±4.4%
183 SEM), sparse in ~ 23% and absent in ~7.5% of the untreated TKO parasites. The cortical MTs
184 are absent in ~ 68% (±6.4% SEM) of the extracellular parasites harvested after ~ 2 hr of cold-
185 treatment (C120). Confirming the synergistic effect of the associated proteins, the cortical
186 microtubules in 75% (±4.5% SEM) of the single knockout mutant *Δtlap2* have wild-type-like
187 arrangement. In contrast, only ~ 4% of the double knockout mutant (*Δtlap2Δspm1*) has a wild-
188 type-like microtubule array. The cortical microtubules are short in ~ 58% (±6.7% SEM), sparse
189 in ~ 29% and absent in ~ 8.7% of this line.
190
191 Because of their stable association with the cortex, it has been hypothesized that the
192 cortical microtubules support the characteristic crescent shape of *Toxoplasma.* We took

advantage of the panel of mutants with varying degrees of defects in the microtubule cytoskeleton and examined their length, width, length-width ratio, and "bowing". Length is defined as the distance from apical to basal tip measured along the arc that passes through both of them and through the center of the parasite, which is given by $2\boldsymbol{r}\tan^{-1}(\boldsymbol{d}/2\boldsymbol{C})$ in Figure 2C. Bowing is a measurement related to curvature (see Figure 2C and Methods for definition). Because apparently straight parasites may be curved but viewed from the wrong direction, measurements were done on the most obviously bowed parasites for each line. The lengths of the microtubule mutants are slightly shorter than that of the wild-type parasite (Table 1). There is not a consistent correlation between microtubule defects and the width or length-width ratio of the parasite. The one parameter that stood out was the bowing index, which is significantly lower in the TKO parasite (1.07± 0.03 µm) than in all the other lines (1.37-1.42 µm) (Table 1). Interestingly, while the *Δtlap2Δspm1* parasite is much more similar in bowing to the RH*Δhx* parental (1.37 vs 1.42 µm) than to TKO parasites, the structural defect of the microtubule array in the *Δtlap2Δspm1* is very pronounced and quite similar to that of the TKO (Fig 2B). This indicates that the effect of the structure of the microtubule array on parasite shape is likely to be nonlinear.

The trajectory of movement of the TKO mutant is more linear than that of the wild-type parasite in 3-D Matrigel

In wild-type parasites, the stable, spirally arranged cortical microtubules have been proposed to guide directionality of parasite movement (Stadler et al., 2017) or to function as a spring that transmits energy to drive gliding motility (Pavlou et al., 2020). We tested these hypotheses by comparing the 3-D motile behaviors of the "wild-type" parent (RH*Δhx*) with those of the TKO parasite, taking advantage of the destabilized and curtailed microtubule array in the TKO. By modifying an established Matrigel-based 3-D motility assay (Leung et al., 2014), we obtained 3-D time-lapse images of the moving parasites under a label-free condition through Differential Interference Contrast (DIC) imaging. DIC imaging not only minimizes phototoxicity, but also enables the observation of parasite morphological changes as they move. However, while fluorescence images exhibit high-contrast that facilitates cell-tracking, automated tracking of cell positions in DIC image stacks is not as straightforward. We applied a series of edge detection filters, followed by erosion and dilation filters on the DIC images to derive images with contrast similar to fluorescence images (Fig 3A-B) that are amenable to 3-D cell tracking. Detection and tracking were carried out using the TrackMate plugin in Fiji, which generates the 3-D coordinates of the cell trajectories for further analysis and 3-D visualization (Fig 3C and Fig 4, Video S1-S4).

To compare the impact of different helically arranged cytoskeletal structures, we also analyzed the motile behavior of a conoid mutant (*Δdcx,* (Nagayasu et al., 2016)) and its "wild-type" parent (RH*ΔhxΔku80*, abbreviated as "RH*Δku80*" (Fox et al., 2009; Huynh and Carruthers, 2009)) in parallel with those of TKO and its RH*Δhx* parent. The conoid is formed of helically arranged tubulin fibers (Hu et al., 2006; Hu et al., 2002; Nagayasu et al., 2016; Swedlow et al., 2002) (Fig 1B). In the *Δdcx* mutant, a structural component (TgDCX) was removed and the conoid structure becomes stunted and disorganized (Nagayasu et al., 2016). We found that on average, the motile percentage of the *Δdcx* is ~31% (486 parasites from 9 independent experiments analyzed), slightly lower than that of its "wild-type" parent ("RH*Δku80*", 404 parasites from 8 independent experiments analyzed) (Table 2). The average net displacement, run-length (i.e., distance between pauses of >5.4 sec) and run speed (average speed during a run) of the *Δdcx* parasite are similar to those of the wild-type

243 parasites (30.4 vs 29.7 μm, ~25.6 vs 24.1 μm and 1.32 vs 1.36 μm/sec, respectively, Fig 4A).
244 As previously reported (Leung et al., 2014), the wild-type parent moves along an irregular
245 helical path. The average dispersal ratio (ratio of net displacement to total distance traveled of
246 motile segments) of the trajectories is 0.74 (a value of 1 indicates a completely linear track).
247 The average turning angle (relative angle of the parasite between two consecutive steps) is
248 ~48°. The trajectories of the *Δdcx* are helical in nature (Fig 4B-C, Video S3-S4), with an
249 average dispersal ratio of 0.69 and turning angle of ~ 52°, indicating slightly tighter turns.
250
251 In contrast, the movement of the TKO parasite was visibly more linear than that of the
252 wild-type parasite (Fig 4B, Video S1-S2). Confirming this visual impression, we found that the
253 dispersal ratio of the TKO parasites is significantly higher than that of the wild-type parent
254 (RH*Δhx*) (0.8 vs 0.73, $p << 0.0001$, Fig 4C). The turning angle of the TKO is significantly lower
255 than the wild-type parasite (~32.5° vs ~ 50°, $p << 0.0001$). Both are consistent with the
256 trajectories being more linear. For segments of trajectories during which the TKO parasite
257 displays near helical movement, the average pitch of the helical turns is significantly longer
258 than that of the wild-type parasite (9.9 μm vs 7.5 μm $p << 0.0001$). Other motility parameters
259 are similar between the two lines. 40.2% of the RH*Δhx* parasites were motile (413 parasites
260 from 6 independent experiments analyzed) (Table 2). ~42.3% of the TKO parasites were
261 motile (395 parasites from 6 independent experiments analyzed). The average net
262 displacement, run-length and run speed are not significantly different between the TKO and
263 RH*Δhx* parasite (32.3 vs 31.2 μm, ~23.1 vs 22.7 μm and 1.39 vs 1.38 μm/sec, respectively,
264 Fig 4A).
265
266 As shown in Figure 1A, there are some remnant cortical microtubules in untreated TKO
267 parasites. To determine whether these remaining microtubules influence the helicity of parasite
268 movement, we cold-treated (CT) the parasites for 2 hr, under which condition the cortical
269 microtubules are nearly fully depolymerized in ~ 70% of the TKO parasites but those in the
270 wild-type parasites are not affected (Fig 1E and Fig 2B). The parasites were then harvested
271 and mixed with Matrigel for 3-D motility assay. The turning angle of the cold-treated TKO (CT-
272 TKO) is nearly the same as that of the untreated TKO parasites (Fig 4B-C). As observed in
273 untreated parasites, the cold-treated TKO parasite moves much more linearly than cold-treated
274 wild-type parasite (CT-RH*Δhx*), as indicated by the significant differences in turn angle (~32.6°
275 vs ~ 50°), dispersal ratio (0.84 vs 0.76), and pitch (10.8 μm vs 8.2 μm).
276
277 To determine the impact of individual microtubule-associated proteins, we examined the
278 3D motility of *Δtlap2, Δtlap2Δspm1* along with the TKO and the wild-type parent (Fig 5). The
279 loss of TLAP2 alone results in a mild defect in the microtubule array (Fig 2B) and a very
280 modest change in the turning angle and dispersal ratio of the movement. The loss of TLAP2
281 and SPM1 together leads to pronounced defects in the microtubule array (Fig 2B) as well as
282 significantly more linear movement as indicated by turning angle and dispersal ratio that are
283 significantly different from the wild-type parent (Fig 5). The alteration in helicity of movement is
284 therefore very much in line with the extent of perturbation of the microtubule array. We note
285 that in this second set of 3D motility experiments, a new batch of Matrigel was used. It is well
286 known that the mechanical properties of Matrigel can vary from batch to batch or change with
287 prolonged storage (Aisenbrey and Murphy, 2020). In the second batch of Matrigel (Fig 5), the
288 turning angles of both wild-type and TKO parasites are much lower than those of the
289 corresponding lines measured earlier (Fig 4C). However, the differences in helicity (turning
290 angle and dispersal ratio) remain highly significant between the mutant and the wild-type
291 parent.

The apical concentration of micronemal vesicles is partially disrupted in the TKO parasite

Critical for effective parasite movement are transmembrane adhesins secreted from the membrane bound vesicles, micronemes (Carruthers et al., 2000; Carruthers and Sibley, 1997; Gras et al., 2017; Huynh and Carruthers, 2006; Rabenau et al., 2001). We have shown previously that micronemal vesicles co-align with the cortical microtubules (Leung et al., 2017). Here we quantify the different patterns of microneme distribution in TKO and its parent (RH*Δhx*). Micronemal vesicles were labeled by immunofluorescence using an antibody that recognizes MIC2, a major adhesin protein (Carruthers et al., 2000; Carruthers and Sibley, 1997; Gras et al., 2017; Huynh and Carruthers, 2006). The micronemal vesicles are enriched in an apical cap region (Fig 6A, 'apical cap conc') in 98% of the wild-type parasites, but only ~ 60% (±4.3% SEM) of the untreated TKO parasite (Fig 6A-B). When cold-treated for 2 hr (C120), this percentage further decreases to ~ 33% (±3.5% SEM) in the TKO parasites. The cold-treatment also has a modest impact on the wild-type parent, with parasites without the apical cap concentration increasing from ~ 2% to ~ 10% (Fig 6B). In parasites that lose the microneme enrichment at the apical cap, an intense concentration of MIC2 labeling remains at the parasite apex (Fig 6A, 'no apical cap conc'). We note that a longitudinal bar is often observed at the parasite apex regardless of whether there is a prominent apical cap of microneme vesicles (Fig 6A, insets). This signal is probably from micronemal vesicles congregating in the conoid as observed by electron microscopy (Aquilini et al., 2021). To investigate whether the secretion of MIC2 is affected, we examined the amount of MIC2 secreted into the supernatant by extracellular RH*Δhx* parental and TKO parasites treated with the calcium ionophore A23187. We found that both lines respond robustly to the calcium ionophore treatment (Fig 6C and Fig S1). The TKO parasite on average secretes MIC2 at ~ 67% of the level of the RH*Δhx* parent (Fig S1), but the difference between the two lines is not statistically significant.

The infection efficiency of the TKO is lower than that of the wild-type parasite, while entry into and calcium-induced egress from the host cell is not affected

Parasite motility is critical for invasion into and egress from the host cell (Dobrowolski et al., 1997; Frenal et al., 2010; Gaskins et al., 2004; Graindorge et al., 2016; Heaslip et al., 2011; Jacot et al., 2016; Meissner et al., 2002; Munera Lopez et al., 2022; Tosetti et al., 2019). In addition, as the cortical microtubules are stable polymers that associate extensively with the parasite cortex, it is conceivable that they might provide mechanical support to the cortex when the parasites penetrate the membrane of the host cell during entry or exit. We therefore used video microscopy to determine whether the destabilization of the cortical microtubules in the TKO parasite might affect any of these processes. To examine parasite egress, the cultures infected by TKO or RH*Δhx* parental parasites were subjected to cold-treatment for 1 hr and then placed at 37°C for egress induced by A23187. Both TKO and wild-type parasites egressed actively and efficiently (Fig 6D, Video S5). Within 150 seconds, egress was completed in >93% of vacuoles for the wild-type parasites and in 100% of vacuoles for the TKO parasites. Of the egressed vacuoles, the average time taken to disperse is ~ 56 seconds for the wild-type parasite (n=14) and ~ 66 seconds for the TKO parasite (n=15) (p value not significant) (Fig 6E). In parallel, we also analyzed the egress behaviors of the *Δdcx* and its RH*Δku80* parent. We found that both lines egressed efficiently (Fig 6E), with an average disperse time of ~ 57.7 and ~ 58.3 seconds for RH*Δku80* (n=15) and *Δdcx* (n=15), respectively.

342 To assess parasite behavior during entry into the host cell, freshly harvested
343 extracellular parasites were settled onto the host cell monolayer by a ~ 10 min pre-incubation
344 on ice and then imaged by DIC at 37°C for 15 min (Fig 6F, Video S6). The number of entry
345 events was recorded for four parasite lines: wild-type RH∆*hx* parental, TKO, wild-type
346 RH∆*ku80* parental, and *Δdcx* parasite. We observed 58 events for RH∆*hx* in 10 videos, 40 for
347 TKO in 13 videos, 56 for RH∆*ku80* in 9 videos, and 35 for ∆*dcx* in 22 videos. The median
348 speed of host cell entry was 25.5 seconds for RH∆*hx*, 22.5 seconds for the TKO, 25 seconds
349 for the RH∆*ku80* and 33 seconds for the ∆*dcx* parasites (Fig 6G). We also did not observe any
350 notable differences among these parasite lines in the morphological changes (*e.g.* the
351 formation and resolution of constrictions) that accompany host cell entry.
352
353 The lower incidence of entry attempts observed in the time-lapse experiments for the
354 TKO and ∆*dcx* indicates lower overall invasion efficiency. Indeed, ∆*dcx* parasites were shown
355 in our previous work (Nagayasu et al., 2016) to invade at a much lower efficiency than the wild-
356 type parasites when invasion was assessed by a 2-color immunofluorescence assay that
357 distinguishes invaded and uninvaded parasites based on different surface antigen accessibility
358 (Carey et al., 2004; Mital et al., 2005). We determined the invasion efficiency of the TKO
359 parasite using a similar approach and found that the TKO parasite invades at ~47 % of the
360 level of its wild-type parent (p= 0.026, unpaired Student's t-tests. # of parasites invaded/field:
361 25.2± 3.2 for RH*Δhx* and 11.8± 1.1 for TKO). Consistent with lower efficiency in invasion, the
362 TKO parasite generates ~ 60% of the number of plaques as the wild-type parasite ($p \approx 0.005$)
363 when examined by a plaque assay, where the parasites were incubated with the host cell
364 monolayer unperturbed for 8 days (Fig 6H). The total area of the host cell monolayer lysed by
365 TKO is 40% of the area lysed by the wild-type parasite ($p < 0.0001$), indicating significantly
366 lower cytolytic efficiency. Thus, regarding the parasite's ability to move helically or conoid
367 structure, host cell entry is less sensitive than overall infection efficiency.
368
369
370 **DISCUSSION**
371
372 The array of cortical microtubules is one of the major features of the cytoskeleton of
373 *Toxoplasma* and other apicomplexan parasites. In *Toxoplasma,* the roots of the cortical
374 microtubules are precisely located at evenly spaced intervals separated by cogwheel-like
375 projections at the circumference of the apical polar ring (Leung et al., 2017; Morrissette and
376 Sibley, 2002a; Nichols and Chiappino, 1987). The cortical microtubules are co-constructed and
377 associated extensively with the inner membrane complex (IMC), guiding its formation during
378 parasite replication (Hu et al., 2002; Morrissette et al., 1997). Inhibition of polymerization in
379 replicating parasites blocks the elongation of daughter microtubules, and results in distorted
380 daughter cortex and failed cell division (Hu, 2008; Hu et al., 2006; Morrissette and Sibley,
381 2002b; Stokkermans et al., 1996). In mature *Toxoplasma*, the cortical microtubules are
382 extraordinarily stable and resistant to drug or cold-temperature treatments that readily
383 depolymerize mammalian microtubules (Hu, 2008; Hu et al., 2006; Morrissette and Sibley,
384 2002b). It was proposed that the cortical microtubules might have various mechanical roles in
385 facilitating parasite motility and invasion (Del Rosario et al., 2019; Pavlou et al., 2020; Stadler
386 et al., 2017). However, the extraordinary stability of these polymers poses a major barrier
387 against directly testing these hypotheses.
388
389 Previously, we generated a mutant (∆*tlap2*∆*spm1*∆*tlap3,* a.k.a."TKO") in which the
390 cortical microtubules are destabilized in the mature parasites while continuing to grow normally

391 in developing daughters (Liu et al., 2015). Here, by quantifying the proportion of TKO parasites
392 with different levels of defects in the array of cortical microtubules, we now have a more
393 complete view of the extent of depolymerization in the non-dividing and dividing parasites. We
394 found that 1) ~ 80% of untreated, non-dividing TKO parasites have severely shortened
395 microtubules and 2) the extent of depolymerization in the mature parasite increases markedly
396 when the daughters start to form, but the development of daughters is not affected. Examining
397 cortical microtubules in the wild-type also revealed a small proportion of mature parasites with
398 shortened cortical microtubules at the end of daughter construction. This suggests that
399 microtubule depolymerization in the mother parasite might be a part of the normal preparation
400 for disassembling maternal structures into component parts for possible recycling in the new
401 generation. The cortical microtubules in mature TKO parasites are likely further sensitized to
402 the depolymerizing activity due to the lack of TLAP2, SPM1, and TLAP3.
403
404 During division, the cortical microtubules of daughters grow continuously and do not
405 display dynamic instability (Hu et al., 2002), indicating that these microtubules are stabilized by
406 associated proteins. TLAP2, SPM1, and TLAP3 are recruited to the cortical microtubules of
407 both mother and daughters (Liu et al., 2015; Tran et al., 2012) (Fig S2), yet they have
408 differential effects on the stability of these two sets of microtubules sharing the same
409 cytoplasm. In the same TKO parasite, while the maternal microtubules are destabilized, the
410 daughter microtubules grow normally. This apparent specific stabilizing activity of TLAP2,
411 SPM1, and TLAP3 for mature cortical microtubules could be because daughter cortical
412 microtubules acquire additional specific stabilizing factors. Of course, for those (hypothetical)
413 factors, we would need to answer how they differentially act on the cortical microtubules of the
414 mother and developing daughters, which coexist in the same cytoplasm.
415
416 When incubated at low temperature, the cortical microtubules in the TKO parasite can
417 be fully depolymerized (Liu et al., 2015). Here we show that this depolymerization is reversible:
418 when the parasite was placed at 37°C after cold-treatment, short cortical microtubules were
419 observed concentrated at the apical end of the parasite. This is consistent with the current
420 hypothesis that the apical polar ring is the nucleating center for the cortical microtubules
421 (Leung et al., 2017; Morrissette and Sibley, 2002a; Nichols and Chiappino, 1987). It is
422 tempting to suggest that the nucleation complexes in the apical polar ring in the mature
423 parasite remain active and are capable of re-nucleating new cortical microtubules after
424 complete depolymerization. However, we cannot exclude the possibility that the new growth
425 occurred from short microtubule stubs that remain associated with the apical polar ring, as a
426 small cap of tubulin antibody labeling remains at the apical end even after prolonged cold
427 treatment. If the latter is true, it suggests differential regulation of stability along the length of
428 the cortical microtubules.
429
430 In the 3-D Matrigel, the TKO mutant moves much more linearly than the wild-type
431 parasite, which travels along a helical path. The stable and spirally arranged cortical
432 microtubules, with their extensive interactions with the cortex, could contribute to the helicity of
433 the parasite movement by maintaining non-isotropic cortical properties (e.g. stiffness), and
434 thus biasing the orientation at which the parasite interacts with its environment. In plant cells,
435 the transmembrane cellulose synthesis complex is dynamically coupled to the cortical
436 microtubules via cellulose synthases interacting (CSI1) protein (Bringmann et al., 2012). This
437 results in the co-alignment of the extracellular cellulose fibers with the cortical microtubules on
438 the other side of the plasma membrane. One could imagine that a similar mechanism might be
439 involved in the confinement of the force-generating actomyosin apparatus associated with the

440 inner membrane complex in *Toxoplasma*, although currently a CSI1-like coupler is unknown.
441 The trajectory of the parasite movement might also be affected by the parasite's shape. For
442 example, in *Plasmodium berghei,* the knockout of IMC1h, which changes the shape of the
443 ookinete, results in more linear movement (Kan et al., 2014). However, in the IMC1h
444 *Plasmodium* mutant, while the cortical microtubules are still present and have a recognizable
445 twist, they are also disorganized, which makes it difficult to disentangle the individual
446 contributions from changes in parasite shape vs in the organization of the microtubules. We do
447 not think the change in parasite shape is the likely explanation for the change in movement
448 trajectory of the *Toxoplasma* microtubule mutants, because there does not appear to be a
449 clear correlation between the parasite shape and linearity of movement. For example, the
450 *Δtlap2Δspm1* parasite, which has a pronounced defect in the cortical microtubule array, moves
451 much more linearly than the wild-type parasite even though their bowing indices are similar.
452
453 We note that while the net displacement, run length and run speed are similar in
454 untreated parental and TKO parasites, these parameters are significantly higher for cold-
455 treated wild-type parasites when compared with those for the cold-treated TKO (Fig 4A). This
456 difference is due almost entirely to a response to the cold-treatment by the wild-type parasite,
457 and the lack of response by the TKO. This lack of response by the TKO parasite indicates that
458 the residual microtubules in the TKO under untreated conditions do not have a notable impact
459 on parasite motility. The increase in speed and persistence of wild-type parasite movement
460 after cold-treatment is not due to a direct effect of the microtubules on motility because 1) the
461 cold-treatment does not have a detectable effect on the microtubule array in the wild-type
462 parasite, and 2) the untreated wild-type parasite, which has a full complement and normal
463 arrangement of cortical microtubules, has the same speed and persistence as the TKO
464 parasite with few microtubules and a disordered array.
465
466 It has been proposed that the cortical microtubules act as a spring to store and release
467 energy for helical gliding (Pavlou et al., 2020). However, our data suggest that these
468 microtubules do not appear to act as a link in any energy relay vital for parasite movement. As
469 discussed above, while the TKO mutant does not move helically, it is clearly capable of
470 sustaining long-distance movement even under conditions where the TKO parasites were pre-
471 treated with cold to nearly fully depolymerize the microtubules. Therefore the cortical
472 microtubules do not play a role in maintaining directional long-distance movement. This means
473 other higher-order structures are needed to limit the direction of force generation by the
474 actomyosin complex. Whatever these structures might be, they need to be regularly arranged
475 and stably associated with the parasite cortex. One candidate is the array of inner membrane
476 particles (IMPs), which form periodic rows of IMPs that run the length along the longitudinal
477 axis of the parasite (Morrissette et al., 1997). A subset of the IMP rows co-align with the
478 cortical microtubules. The depletion of a potential IMP component (GAPM1a) in mature
479 parasites results in decreased parasite displacement in the 3-D Matrigel as well as destabilized
480 and disordered cortical microtubules (Harding et al., 2019). It is worth noting that, in contrast to
481 the GAPM1a mutant, the net displacement of the TKO parasite is similar to that of the wild-
482 type (Fig 4A). This separation of helicity from sustained parasite movement might be due to
483 the cell-stage dependent nature of the stability of the cortical microtubules in the TKO parasite.
484 The IMC cortex of the parasite is built concomitantly with the cortical microtubules during
485 daughter formation. Because the daughter cortical microtubules grow normally in the TKO
486 parasite, the structures in the IMC also likely form largely normally. Thus, we think that, in the
487 mature TKO parasites, we are seeing mainly the impact of the microtubule destabilization
488 itself, which manifests solely in the change from helical to linear movement.

Given the precision by which the cortical microtubules are constructed, the extensive suite of associated proteins (Leung et al., 2017; Liu et al., 2015; Liu et al., 2013; Tran et al., 2012), and their extraordinary stability, we had expected that microtubules would provide important mechanical support for the cortex in the mature parasite. To our surprise, the shape of the TKO parasite is still crescent in nature, and there is also no detectable difference in the behavior of the parasite during host cell entry and egress, when the parasite experiences considerable mechanical stress pushing through the host cell cortex. This indicates that other cortical structures, such as the inner membrane complex and associated intermediate filament-like network, are more important as structural support in mature parasites. Notably, the conoid structure mutant, Δ*dcx,* which invades with a much lower efficiency (Nagayasu et al., 2016), also showed wild-type like behavior during entry. This suggests that host cell entry is considerably less sensitive to the change in the structure of the cortical microtubules and conoid compared with extracellular migration during infection.

Lastly, TLAP2, SPM1, and TLAP3, the three proteins collectively responsible for the stability of cortical microtubules in mature *Toxoplasma*, have well-conserved orthologs in *Plasmodium* spp (Liu et al., 2015). It would be intriguing to determine whether the microtubule stabilizing function of these proteins, and the influence of cortical microtubule stability on parasite movement are also conserved among the apicomplexans. As the cortical microtubules in the developing daughter and the mature TKO parasites display distinct polymerization and depolymerization states, identifying the activities responsible for this maternal-filial distinction will generate insights into how the cortical microtubules of the mother and developing daughters (composed of the same polymer and less than half a micron apart) coexist in distinct biochemical states and how the switch from one state to the other occurs as the daughters become mature.

MATERIALS AND METHODS

T. gondii mutant strains and host cell cultures

Host cell and *T. gondii* tachyzoite parasite cultures were maintained as described previously (Leung et al., 2017; Liu et al., 2015; Munera Lopez et al., 2022; Roos et al., 1994). The TKO (Δ*tlap2*Δ*spm1*Δ*tlap3*), Δ*tlap2*Δ*spm1*, Δ*tlap2* mutants and the *mEmeraldFP-TLAP2* knock-in parasite were reported in (Liu et al., 2015). The Δ*dcx* parasite was reported in (Nagayasu et al., 2016).

Temperature treatment of T. gondii for testing microtubule stability

Cultures of intracellular parasites growing in HFF cells plated in 3.5-cm glass-bottom dishes (MatTek Corporation, CAT# P35G-1.5-14-C or CAT# P35G-1.5-21-C) were incubated at 7°C for 20, 60, 90 or 120 min in L15 imaging media, which is Leibovitz's L-15 (21083-027, Gibco-Life Technologies, Grand Island, NY) supplemented with 1% (vol/vol) heat-inactivated cosmic calf serum (CCS; SH30087.3; Hyclone, Logan, UT). For recovery, the cultures incubated at 7°C for 2 hours were subsequently placed at 37°C for 5, 10, 20, 30, 60 or 120 min in L15 imaging media. The samples were then processed for immunofluorescence as described below. Total number of intracellular parasites analyzed: 444, 422, 468, 423 of TKO and 246, 274, 300, 390 of wild-type cold-treated at 7°C for 20, 60, 90 or 120 min, respectively; 440, 428, 456, 496, 396, 360 of TKO, and 295, 168, 172, 166, 205, 230 of wild-type recovered at 37°C for 5, 10, 20, 30, 60, or 120 min, respectively.

540 *Immunofluorescence*
541
542 All steps of the immunofluorescence labeling were performed at room temperature. For
543 microtubule labeling of intracellular parasites (Fig 1), *T. gondii*–infected HFF monolayers
544 growing in glass-bottom dishes were fixed in 3% (vol/vol) formaldehyde and 50% (vol/vol)
545 methanol in 0.5X PBS for 15 min, permeabilized in 0.5% (vol/vol) Triton X-100 (TX-100) in
546 PBS for 15 min, washed with PBS twice, followed by incubating with the primary antibody
547 (mouse monoclonal anti-acetylated tubulin, 6-11B-1, 1:1000, Sigma T6793) and then with the
548 secondary antibody (goat anti-mouse IgG- Alexa Fluor 488, A11029, Molecular Probes) at
549 1:1000, for 1 hr each. For labeling of the Inner Membrane Complex Protein 1 (IMC1), the
550 samples were subsequently blocked with 1.5% BSA in PBS for 1 hour, then incubated for 1
551 hour with rabbit anti-IMC1 (a kind gift from Dr. Con Beckers, William Carey University) at
552 1:1000, and finally with goat anti-rabbit IgG -Alexa Fluor 568 (A11036, Molecular Probes) at
553 1:1000 for 1 hour. The antibodies were diluted in the blocking solution (i.e. 1.5% BSA in PBS).
554
555 For microtubule labeling of extracellular parasites (Fig 2), parasites were harvested as
556 described in (Munera Lopez et al., 2022). To collect cold-treated parasites, cultures with
557 intracellular parasites were placed at ∽ 7ºC for 2 hr as described above before harvesting.
558 After harvesting, parasites were suspended in 3% (vol/vol) formaldehyde and 50% (vol/vol)
559 methanol in 0.5X PBS and allowed to settle to the glass-bottom of the MatTek dishes for 15
560 min. The samples were then processed as described above for the intracellular parasites.
561
562 Immuofluorescence labeling of intracellular parasites with a mouse anti-TgMIC2 antibody,
563 6D10 (Carruthers et al., 2000) (a kind gift from Dr. Vern Carruthers, University of Michigan)
564 was carried out as described in (Munera Lopez et al., 2022). A rabbit anti-GAP45 antibody (a
565 kind gift from Dr Con Beckers, William Carey University) at 1:2000, followed by a goat anti-
566 rabbit IgG- Alexa Fluor 488, (A11034, Molecular Probes) at 1:1000, was used to label the
567 parasite cortex in these experiments (Fig 6A).
568 The labeling of the mEmeraldFP-TLAP2 knockin parasite with a mouse anti-ISP1 antibody (a
569 kind gift from Dr. Peter Bradley, University of California, Los Angeles, (Beck et al., 2010)) (Fig
570 S2) was carried out as described in (Liu et al., 2015).
571
572 *Three-dimensional structured-illumination microscopy*
573
574 Three-dimensional structured-illumination microscopy (3D-SIM) image stacks were collected at
575 z-increments of 0.125 µm using a DeltaVision OMX Flex imaging station (GE Healthcare-
576 Applied Precision). A 60x oil immersion lens (numerical aperture [NA] 1.42) and immersion oil
577 at refractive index 1.520 were used. Structured illumination image reconstructions and 3D
578 projections were processed using the functions and software supplied by the manufacturer.
579
580 *Replication assay*
581
582 The intracellular replication assay was performed as described in (Heaslip et al., 2011). Four
583 independent experiments were performed. In each replicate, the number of parasites in ~ 100
584 vacuoles was counted for each strain at each time point.
585
586 *Shape analysis*
587 Parasites were harvested from a heavily infected T12.5 flask of HFF by scraping, passing the
588 suspension through a 23G needle, and filtering through a 3µm pore size filter. The suspension
589 was centrifuged at 1500 x g for 3 min, the pellet was suspended 1 ml of L15 media containing
590 1% calf serum, and then centrifuged at 3500 x g for 2.5 min, discarding all but ~20 µL of the

supernatant, which was used to resuspend the pellet. 10-15 µL of the concentrated parasite suspension was spread on a slide and covered with a coverslip. DIC images were collected as z-stacks of 7 to 19 slices in 0.8µm z-steps, using a 60x NA 1.3 silicon immersion lens. A custom script in the image processing software Semper (Saxton, 1996) was used to display the image, choose the best-focus z-layer, and pick parasites. The most obviously bowed parasites were selected for measurement because apparently straight parasites could be curved but viewed from the wrong direction. For each chosen parasite, shape parameters were calculated using the following manually identified features.

First, for each parasite image, a line was drawn from apical tip to basal tip. The coordinates of this line, with length denoted ***d***, were used to redisplay an enlarged image of the chosen parasite with the drawn line vertical, apical tip upwards. On this enlarged, re-oriented image, first the left, then the right-hand edge of the parasite was marked. Denote the distance from the apical-basal line to the left-hand border by ***a***, to the right-hand border by ***b***. Distances to the right of the line are positive, to the left are negative. The width of the parasite at its midpoint is given by ***b*** - ***a***, with ***a*** and ***b*** signed as defined. Length and bowing indices were then calculated from the coordinates of the marks as follows (see Figure 2C).

The "bowing", defined as the distance, ***B***, from the drawn apical-basal line to the center (defined as half-way between the left-hand and right-hand edges) of the parasite is given by (***a*** + ***b***)/2, where ***a*** and ***b*** are signed numbers as defined above. Now consider an arc of an imaginary perfect circle that passes through the center of the parasite as well as through the endpoints of the previously drawn apical-basal line. Let ***C*** be the distance from the center of that circle to the midpoint of the apical-basal line, measured perpendicularly. Consider two radii, length ***r***, of that circle, one from the center of the circle to the apical tip of the parasite, the other from the center of the circle to the midline of the parasite. Referring to the diagram in Figure 2, it will be seen that for the first radius, $r^2 = (d/2)^2 + C^2$, and for the second radius $r^2 = (B + C)^2$. Solving for ***C*** gives $C = [(d/2)^2 - B^2]/2B$, and ***r*** is then calculated as ***B*** + ***C.***
If the parasite were not bowed at all, then the parasite length would be exactly ***d***.
We define the length (***L***) of the parasite to be the distance from apical to basal tip measured along the arc that passes through both of them and through the center of the parasite, which is given by $2r \tan^{-1}(d/2C)$.

3-D motility assay and image acquisition

The 3-D motility assay for *Toxoplasma,* originally developed in (Leung et al., 2014), was carried out largely as described in (Munera Lopez et al., 2022). The environmental controller of a DeltaVision OMX Flex imaging station (GE Healthcare-Applied Precision) was set to heat the stage and objective lens at 37°C and allowed to equilibrate for >30 mins. A flow chamber was assembled as described in (Munera Lopez et al., 2022), then placed onto the heated stage at least 10 minutes before imaging. For cold-treated parasites, cultures with intracellular parasites were placed at ~ 7ºC for 2 hr, before harvesting as described in (Munera Lopez et al., 2022). The harvested parasite suspension was kept on ice for ~30 sec, then mixed with an equal volume of Matrigel (Corning, 356237) on ice and pipetted into the pre-heated flow chamber. The chamber was then sealed with a polymerizable liquid silicone rubber (Nobilium Inc, Nobilsil #7453+7434) and image acquisition was started within ~2-3 mins after the suspension had entered the 37°C chamber.

For each imaging experiment, 151–181 image stacks were acquired at 1.36 sec intervals (7 msec exposure per optical section). Each stack consisted of 41 optical sections,

spaced 1 µm apart in the Z-plane (40 µm stacks), with field of view of 1500×1500 pixels, binning 2×2, with a final dimension of 750 × 750 pixels. Image stacks were acquired from at least ∽10 µm above the coverslip.

To represent the 3-D DIC images in 2-D format (Fig 3 and Video S1&3), we performed focus-stacking using Fiji by applying the Extended Depth of Field Sobel Projection plugin from (Forster et al., 2004; Schindelin et al., 2012)

DIC image stacks processing and cell tracking

DIC images were processed using our custom scripts extended from (Munera Lopez et al., 2022). High contrast images were generated by subjecting the DIC images to 1) a 3-D median filter (kernel nx = ny = nz = 2 px) to reduce noise, 2) a 2-D Laplacian filter to attenuate out-of-focus portions of the cells, and 3) a 3-D gradient filter of Sobel type for edge detection. A dilation and erosion process using a maximum filter followed by a minimum filter (kernel nz = 3 px, nx = ny =13 px) was then applied. 2 pixels from all x and y edges were cropped before tracking to avoid edge artifacts. We implemented the imaging filters using Python 3 to enable GPU-acceleration using the CuPy plugin (Harris et al., 2020; Okuta et al., 2017; Van Rossum, 2009). The TrackMate plugin in Fiji was then used to detect and track the parasites in the processed image stacks (Ershov et al., 2022; Schindelin et al., 2012; Tinevez et al., 2017). The Difference-of-Gaussian (DoG) detector was employed for spot detection with a diameter of 7 μm. To avoid artifacts associated with edge-effects and out-of-focus signal, we excluded spots detected within the first and last 1 μm of the z-dimension and 3 μm of each of the x and y dimension. The Kalman filter tracker was used to reconstruct the cell tracks, and false reconstructions (i.e., “tracks” between debris or random noise) were filtered out based on quality, track length, and duration. The values for these parameters were determined empirically. The resulting tracks were manually verified and errors such as misdetections and gaps were corrected by adding or deleting individual spots. To refine spot positions, we used the TrackMate spot fitting feature to fit a 3-D Gaussian with fixed radius on each spot. After conducting a second round of manual verification, we then separated the motile parasite tracks from the non-motile tracks by applying another set of filters based on displacement and speed. The 3-D coordinates of both the non-motile and motile tracks were copied to different comma-separated value text files (.csv) for analysis in R version 4.1.2 in RStudio (RStudioTeam, 2020; Team, 2021).

Trajectory analysis

We used the R package celltrackR v 1.1.0 and our own custom functions to process and analyze the parasite trajectories (RStudioTeam, 2020; Team, 2021; Wortel et al., 2021). The complete list of the rest of the R packages we used for our analysis is at the end of this section. First, the global drifts in the data were corrected according to the workflow developed by (Wortel et al., 2021) and we calculated the drift velocity from the corresponding set of non-motile tracks. Then, non-motile ends (the very start or very end) of the parasite trajectories were trimmed to eliminate biases introduced by the asynchronous nature of the parasite motility. After trimming, only tracks with more than four steps (i.e., five tracking points) were included in the subsequent analysis.

In Figures 4 and 5, the net displacement is a simple Euclidean distance between the first point and the last point of the trajectories. The run length is the total distance traveled between two “pauses”, which we defined as an event when the parasite stops moving for more

691 than 5.4 sec (>= 4 frames). "stop moving" means that the speed of a step (sub-track of length
692 1) is lower than a threshold. For each data set, the threshold value was calculated by taking
693 the average step-speed of the non-motile tracks. We removed the track points that correspond
694 to pause events, introducing gaps. The motile segments were then obtained by splitting the
695 tracks around those gaps. The run speed was obtained by dividing a motile segment's total
696 distance (run length) by its total duration. For Figures 4C and 5, the dispersal ratio was
697 calculated by taking the net displacement of the motile segments and dividing it by the run
698 length, where a value of 1 indicates a completely linear track.
699
700 For analyzing the turning angle (Fig 4C and Fig 5), any stops that were not filtered out
701 before (i.e., stops that lasted less than 4 frames) and steps with displacement of less than 10%
702 of the parasite body length (~ 0.75 μm) were cut out from the motile segments before splitting
703 into sub-segments. Sub-segments that are less than 3-frames long were excluded from the
704 turning angle analysis, which was done based on (Wortel et al., 2021).
705
706 The pitch length is the displacement associated with one complete helical turn, which
707 was quantified as the straight-line distance between the starting and ending points of the turn.
708 These points were identified through visual inspection of the trajectories and parasite
709 orientation in 3-D space for the pitch calculation in Fig 4C.
710
711 The 3-D reconstruction of the processed DIC image stacks, along with the tracks
712 exported from TrackMate (Fig 3C, Fig 4B, Video S1-S4), was done using the 3-D viewer and
713 Track Processor in Icy (de Chaumont et al., 2012). Gaussian blur with a sigma of 2 was
714 applied to the processed stacks before Icy rendering.
715
716 Outliers were removed from the datasets before performing statistical analysis. For
717 each measured variable (Fig 4A&C, Fig 5), all the data points were combined to calculate the
718 first (Q1), third (Q3) quartiles, and interquartile range (IQR). A data point is defined as an
719 outlier if it is 1.5 times the IQR greater than the Q3 or 1.5 times the IQR less than the Q1.
720
721 The Kruskal-Wallis test was done to compare the groups for all of the track
722 measurements in Figures 4A&C and Figure 5 (RStudioTeam, 2020). We used R version 4.1.2
723 (Team, 2021) and the following R packages: data.table v. 1.14.6 (Dowle and Srinivasan,
724 2022), gridExtra v. 2.3 (Auguie, 2017), onewaytests v. 2.7 (Dag et al., 2018), pracma v. 2.4.2
725 (Borchers, 2022), rmarkdown v. 2.20 (Allaire et al., 2023; Xie et al., 2018; Xie et al., 2020),
726 rstatix v. 0.7.2 (Kassambara, 2023), scales v. 1.2.1 (Wickham and Seidel, 2022), tidyverse v.
727 2.0.0 (Wickham et al., 2019).
728
729 *MIC2 secretion assay*
730
731 To examine microneme secretion, freshly egressed parasites were harvested. $4x10^7$ parasites
732 were resuspended in 90 µl DMEM with 1% bovine calf serum, incubated at 10 min at 37 ºC
733 with or without 5 μM A23187, placed on ice for 5 min, and centrifuged for 10 min at ~ 800 g to
734 separate the secreted fraction (supernatant) from the parasites (pellet). The supernatant (40
735 µl) and pellet fractions were analyzed by Western blot as described in (Leung et al., 2019) with
736 a mouse 6D10 anti-TgMIC2 antibody (Carruthers et al., 2000) at 1:1000 dilution, a mouse anti-
737 tubulin (Sigma, T6074) at 1:4000 dilution, and a Donkey anti-mouse IRDyE 680RD (Li-cor
738 #926-68070) at 1:7000 as secondary antibody. To normalize A23187-induced MIC2 secretion,
739 background-subtracted fluorescence of the MIC2 band from the supernatant sample was

divided by background-subtracted fluorescence of the tubulin band in the corresponding pellet sample.

Egress assay

For induced egress assay, parasites were added to MatTek dishes containing a confluent HFF or BS-C-1 monolayer and grown for ~ 35 hours. Cultures were washed once and incubated in 2 ml of L15 imaging media and placed at ~7°C for 1 hr, before being moved to the environmental chamber kept at 37ºC. The media was then replaced with ~ 2 ml of 5 μM A23187 in L15 imaging media. Images were collected at 37ºC with 1 sec interval for 10 minutes on an Applied Precision Delta Vision imaging station equipped with an environmental chamber.

Invasion assays

To analyze the behavior of live parasites during invasion, extracellular parasites were used to infect a MatTek dish containing a nearly confluent monolayer of HFF cells. The dishes were incubated on ice in L15 imaging media for ~10 min to facilitate parasite settling on the host cells. The culture was then imaged at 37°C with 1 sec intervals for 15 min to capture invasion events.

Immunofluorescence-based invasion assays were carried out as described in (Munera Lopez et al., 2022) with some modifications. ~$4x10^6$ freshly egressed parasites were used to inoculate a MatTek dish of nearly confluent HFF cells. After 10 min incubation on ice and then 10 min incubation at 37°C, the samples were processed for immunofluorescence. Three biological replicates, each with three technical replicates, were performed. Parasites in 15 fields were counted for each strain per technical replicate. In total (intracellular + extracellular), 4852 parasites were counted for the RH*Δhx* parent and 2944 for the TKO parasite. P-values were calculated by unpaired Student's t-tests for the biological replicates.

Plaque assays

A total of 50, 100 and 150 freshly harvested parasites were added to each well of 6-well plates containing confluent HFF monolayers and grown undisturbed for 8 days at 37°C, then fixed with 70% ethanol for 15 min and stained with 1% (wt/vol) crystal violet in 25% (vol/vol) methanol, rinsed with PBS, air-dried, and imaged.

Acknowledgments
We are grateful to Dr. Owen Saxton (University of Cambridge, United Kingdom) for providing the source code for his 'Semper' image processing package, Dr. Con Beckers (William Carey University, Mississippi) for the rabbit anti-TgIMC1 and anti-TgGAP45 antibodies, Dr. Peter Bradley (University of California, Los Angeles) for the mouse anti-TgISP1 antibody, and Dr. Vern Carruthers (University of Michigan, Ann Arbor) for the mouse mAb 6D10 anti-TgMIC2 antibody. We thank Melissa Molina for tissue culture support.

Conflict of Interest Statement
The authors declare that they have no conflict of interest.

Funding: This study was supported by funding from the National Institutes of Health/National Institute of Allergy and Infectious Diseases (R01-AI132463) awarded to K.H.

Figure Legends

Figure 1. Cortical microtubules in intracellular mature TKO (*Δtlap2Δspm1Δtlap3*) and wild-type (RH*Δhx*) parasites.

A. Projections of image stacks acquired by three-dimensional structured illumination microscopy (3D-SIM) of the non-dividing wild-type (RH*Δhx*) and TKO parasites. While 100% of the wild-type parasites have the typical spirally arranged full microtubule array, ~79% (±8.5% STDEV) of the TKO parasites have significantly curtailed/short microtubules. The cortical microtubules are sparse in the other 21%. Green and grayscale: tubulin labeling by a mouse anti-acetylated tubulin antibody, which also labels the microtubules in the host cell (arrowhead). Magenta: cortex labeling by a rabbit anti-IMC1 antibody. Arrowheads: host cell microtubules.

B. Diagrams of wild-type parasites at the initiation (INT), elongation (EL), pre-emergence (pre-EM), and emergence (EM) stages of daughter construction. Cortical microtubules and the conoid are shown for the mother and daughter parasites.

C. *Left*: Projections of 3D-SIM images of TKO and wild-type parasites at the initiation, elongation, pre-emergence, and emergence stage of daughter construction. Hollow arrows: cortical microtubules in the mother parasite. Arrows: daughter parasites. Arrowheads: host cell microtubules. Insets (0.7X) are projections that include a subset of the image stack (sub pj) to better display the structure of the daughter parasites, which are obscured in the full projections (full pj) for the wild-type parasites due to the cortical microtubules in the mother. Note that for the TKO parasite, due to the shortness or complete absence of the maternal microtubules, the daughters are as fully visible in the full projection as in the subset projection.

Right: Quantification of the proportions of wild-type (top) and TKO (bottom) parasites that display various characteristics in the maternal cortical microtubule array at different stages, including the non-dividing (non-DIV) stage or the initiation (INT), elongation (EL), pre-emergence (pre-EM), and emergence (EM) stages of daughter construction. For the TKO parasites, the two patterns observed are "short or sparse" (*i.e.* similar to non-dividing TKO parasites) and "absent". For the wild-type parasites, the two patterns observed are "non-dividing wild-type-like" or "short or sparse". Error bars: standard error from three independent experiments. Total number of parasites analyzed: 88, 68, 50, 36 of TKO and 52, 62, 54, 49 of wild-type at the initiation, elongation, pre-emergence, or emergence stage, respectively. The data for the non-dividing stage is the same as shown in Fig 1A.

D. Average number of cell divisions at 12, 24 or 36 hrs after infection in four independent experiments for RH*Δhx* (WT) and TKO parasites. Error bars: standard deviation

E. *Left*: Quantification of the percentage of non-dividing wild-type (RH*Δhx*) and TKO parasites that display various characteristics in the array of the cortical microtubules after being placed at ~ 7°C for 0, 20, 60, 90 or 120 min (C0-C120) as well as after recovery at 37°C for 5, 10, 20, 30, 60, or 120 min after 120 min of ~ 7°C incubation (R5-R120). For the TKO parasites, the two patterns observed are "short or sparse" or "absent". For wild-type parasites, the cortical microtubules remain similar to those in untreated parasites under all conditions tested here (after cold-treatment and cold-treatment plus 37°C recovery). Error bars: standard error from three independent experiments. *Middle*: projection of 3D-SIM images of TKO parasites in which cortical microtubules are absent. *Right*: projection of 3D-SIM images of TKO parasites after 1hr of 37°C (R60) recovery, in which short cortical microtubules at the apical end are seen. Arrowhead: host cell microtubules.

Figure 2. Comparison of cortical microtubule morphology and shape of extracellular wild-type parental (RH*Δhx*), *Δtlap2, Δtlap2Δspm1,* and TKO (*Δtlap2Δspm1Δtlap3*) parasites

840 **A.** Projections of image stacks of wide-field deconvolved images of extracellular RH*Δhx* and
841 TKO (*Δtlap2Δspm1Δtlap3*) parasites with (C120) and without cold-treatment. Green and
842 grayscale: tubulin labeling by a mouse anti-acetylated tubulin antibody. Magenta: cortex
843 labeling by a rabbit anti-IMC1 antibody. Insets: Grayscale images of the tubulin labeling in a
844 few parasites in each field displayed at 3X magnification. Dotted outlines were drawn based on
845 IMC1 labeling.
846 **B.** Quantification of the proportions of extracellular RH*Δhx*, *Δtlap2, Δtlap2Δspm1,* and TKO
847 (*Δtlap2Δspm1Δtlap3*) parasites that display various characteristics in the cortical microtubule
848 array. "Short", "sparse", and "absent" phenotypes are as defined in Figure 1. The
849 "Intermediate" phenotype refers to arrays with detectable gaps but less severe than the
850 "sparse" arrays. For RH*Δhx* and TKO parasites, measurements of parasites harvested after 2
851 hr (C120) of cold treatment are also included. Error bars: standard error.
852 **C.** *Top:* Illustration for the calculation of length, width, and bowing of extracellular parasites.
853 *Bottom*: diagrams and sample images of parasites that have different bowing indices.
854 Quantification of length, width, and bowing of extracellular RH*Δhx*, *Δtlap2, Δtlap2Δspm1,* and
855 TKO (*Δtlap2Δspm1Δtlap3*) parasites are included in Table 1.
856
857 **Figure 3.** Workflow for image processing and automatic tracking of 3-D motility data acquired
858 by DIC imaging
859 **A.** Schematic diagram of the image processing (pink outline and box), detection and tracking
860 (blue outline), and tracks analysis (black outline) workflow for 3-D motility data acquired by DIC
861 imaging. (pink) A representative area of a slice from a DIC image stack before processing and
862 the resulting images corresponding to the filters applied on each processing step using
863 Python3, showing the resulting high contrast image. For details, see Materials and Methods
864 section.
865 **B.** Focused composite image of a DIC image stack (41 slices; 40 *μ*m) of extracellular wild-type
866 parasites in Matrigel and corresponding processed image (represented by its maximum
867 projection) (see also Video S1).
868 **C.** Examples of 3-D tracks for motile RH*Δhx* parental, TKO, RH*Δku80* parental and *Δdcx*
869 parasites reconstructed in the Icy software (see also Video S1- S4). Length of arrows = 16 μm.
870
871 **Figure 4.** The 3-D trajectories of TKO parasites are more linear than those of parental
872 parasites.
873 **A.** Frequency distribution and statistical analysis of motion-related parameters including net
874 displacement, run length (distance between pauses >5.4 sec), and run speed of RH*Δhx*
875 parental and TKO without or with cold-treatment (CT), and RH*Δku80* parental and *Δdcx*
876 parasites. For cold-treated TKO, intracellular parasite cultures were placed at 7 degree for two
877 hours before harvesting. For the other samples/conditions, the parasites were harvested as
878 described previously in (Munera Lopez et al., 2022). All motility assays were carried out at
879 37°C.
880 **B.** Representative tracks projected on the (x, y) plane with superimposed origins (red circles)
881 for RH*Δhx* parental and TKO without or with cold-treatment (CT), and RH*Δku80* parental and
882 *Δdcx* parasites. Enlarged insets (4X) include the segments indicated by the dashed boxes in
883 the trajectories. Scale bars: 10 *μ*m.
884 **C.** Frequency distribution and statistical analysis of helicity-related parameters including
885 turning angle, dispersal ratio, and the pitch of RH*Δhx* parent and TKO, without or with cold-
886 treatment (CT). An illustration defining pitch is included. Data for all parameters are also
887 displayed for RH*Δku80* parental and *Δdcx* parasites except for the pitch.
888 The mean values for individual histograms in A and C are shown at the top (in red) and also

889 marked by the dashed line. P-values (in brackets under the mean values) were calculated by
890 the Kruskal-Wallis test. ns: not significant.
891
892 **Figure 5.** Comparison of 3-D motility of wild-type parental (RH*Δhx*), *Δtlap2, Δtlap2Δspm1,* and
893 TKO (*Δtlap2Δspm1Δtlap3*) parasites.
894 Frequency distribution and statistical analysis of net displacement, run length, run speed,
895 turning angle and dispersal ratio of RH*Δhx*, *Δtlap2, Δtlap2Δspm1,* and TKO
896 (*Δtlap2Δspm1Δtlap3*) parasites.
897 Mean values for individual histograms are shown at the top (in red) and also marked by the
898 dashed line. P-values (in brackets under the mean values) were calculated by the Kruskal-
899 Wallis test.
900
901 **Figure 6.** The speeds of entry and egress of TKO parasites are similar to those of parental
902 parasites despite altered localization of micronemal vesicles, and lower invasion and plaquing
903 efficiency
904 **A.** Projections and single sections of 3D-SIM images of representative intracellular parasites
905 with and without an apical cap concentration of micronemal vesicles. Images of RH*Δhx*
906 parasites and TKO parasites are used as examples for "apical cap concentration" and "no
907 apical cap concentration", respectively. Green and grayscale: microneme labeling by a mouse
908 anti-MIC2 antibody. Magenta: cortex labeling by a rabbit anti-GAP45 antibody. Insets (shown
909 at 2X, contrast enhanced to display weaker signals) include apex regions of parasites
910 indicated by arrowheads. A longitudinal bar of MIC2 labeling at the apex is observed.
911 **B.** Quantification of the percentage of RH*Δhx* parental and TKO parasites that have an apical
912 concentration of micronemal vesicles. Three conditions are included: no treatment, and
913 treatment at ~ 7°C for 60 (C60) or 120 min (C120) prior to the immunofluorescence labeling. P-
914 values were calculated by unpaired Student's t-tests.
915 **C.** Western blots of the secreted (supernatant, S) and unsecreted (pellet, P) fractions of
916 RH*Δhx* and TKO parasites with (+) or without (-) A23187 treatment. The blot was probed by
917 antibodies against MIC2 and tubulin. The sizes of molecular weight markers (M) are indicated
918 in kDa on the left. The contrast for images of the Western blot is enhanced and inverted to aid
919 visualization of the bands. Please see Fig S1 for the full blot.
920 **D.** Images selected from time-lapse experiments of intracellular RH*Δhx* parental and TKO
921 parasites treated with 5 *μ*M A23187 (also see Video S5). Parasitophorous vacuoles are
922 indicated by the arrows. The RH*Δhx* parental and TKO parasite cultures were placed at ~ 7°C
923 for 1 hr prior to the egress experiment, which was conducted at 37°C.
924 **E.** Dot plots of time taken to disperse after treatment with 5 *μ*M A23187 for RH*Δhx* parental,
925 TKO, RH*Δku80* parental and *Δdcx* parasites. P-values were calculated by unpaired Student's
926 t-tests. ns: not significant.
927 **F.** Images selected from time-lapse recording of RH*Δhx* parental, TKO, RH*Δku80* parental and
928 *Δdcx* parasites in the process of invasion (also see Video S6). Frames marked in yellow: entry
929 completed. Green arrows: constrictions formed during invasion.
930 **G.** Dot plots of time taken for entry (i.e. time from parasite contact with the host cell at its apical
931 end to completion of entry) for RH*Δhx* parental, TKO, RH*Δku80* parental and *Δdcx* parasites.
932 P-values were calculated by unpaired Student's t-tests. ns: not significant.
933 **H.** *Top*: Plaques formed by the RH*Δhx* parental and TKO parasites. "plaques" are areas of the
934 host cell culture lysed by repeated cycles of parasite invasion, replication, and egress.
935 *Bottom*: Bar graphs that compare the number of plaques (left) and total plaque area (right) of
936 the RH*Δhx* parental and TKO parasites. Five independent experiments were conducted. Error
937 bars: standard error. P-values were calculated by unpaired Student's t-tests.

938 **Table 1.** Quantification of length (L), width (W), length to width ratio (L/W), and Bowing (B) for
939 four *T. gondii* strains. SEM: Standard error of the mean. P-values comparing the mutant strains
940 (*Δtlap2, Δtlap2Δspm1,* and the TKO) with the RHΔ*hx* parent are from unpaired Student's t-
941 tests.
942

Parasite strain (Total number of parasites analyzed)	L (µm) ± *SEM* p value	W (µm) ± *SEM* p value	L/W ± *SEM* p value	B (µm) ± *SEM* p value
RHΔ*hx* (252)	7.32± 0.06	2.05± 0.01	3.59± 0.03	1.42± 0.02
Δ*tlap2* (207)	7.09±0.04 **p = 0.002**	1.91± 0.01 **p < 0.0001**	3.74± 0.03 **p = 0.001**	1.42± 0.02 p = 0.99
Δ*tlap2*Δ*spm1* (151)	7.09± 0.04 **p = 0.004**	2.02± 0.02 p = 0.20	3.55± 0.03 p = 0.39	1.37± 0.02 p = 0.10
TKO Δ*tlap2*Δ*spm1*Δ*tlap3* (181)	7.04± 0.05 **p = 0.0007**	2.14± 0.02 **p = 0.0003**	3.33± 0.03 **p < 0.0001**	1.07± 0.03 **p < 0.0001**

943
944
945
946
947 **Table 2. Fraction of motile parasites in the 3-D motility assay**
948

Parasite strain	Mean percent motile ± SEM (# of independent replicates)	Total number of parasites analyzed
RHΔ*hx* (TKO parent)	40.2 ± 6.4 (*N=6*)	413
TKO (Δ*tlap2*Δ*spm1*Δ*tlap3*)	42.3 ± 6.8 (*N=6*)	395
RHΔ*hx*Δ*ku80* (Δ*dcx* parent)	36.5 ± 4.08 (*N=8*)	404
Δ*dcx*	30.9 ± 5.0 (*N=9*)	486

949
950
951

REFERENCES

Aisenbrey, E. A. and Murphy, W. L. (2020). Synthetic alternatives to Matrigel. *Nat Rev Mater* **5**, 539-551.

Allaire, J. J., Xie, Y., McPherson, J., Luraschi, J., Ushey, K., Atkins, A., Wickham, H., Cheng, J., Chang, W. and Iannone, R. (2023). {rmarkdown}: Dynamic Documents for R.

Aquilini, E., Cova, M. M., Mageswaran, S. K., Dos Santos Pacheco, N., Sparvoli, D., Penarete-Vargas, D. M., Najm, R., Graindorge, A., Suarez, C., Maynadier, M. et al. (2021). An Alveolata secretory machinery adapted to parasite host cell invasion. *Nat Microbiol*.

Auguie, B. (2017). {gridExtra}: Miscellaneous Functions for "{Grid}" Graphics.

Bannister, L. H. and Mitchell, G. H. (1995). The role of the cytoskeleton in Plasmodium falciparum merozoite biology: an electron-microscopic view. *Annals of tropical medicine and parasitology* **89**, 105-11.

Beck, J. R., Rodriguez-Fernandez, I. A., de Leon, J. C., Huynh, M.-H., Carruthers, V. B., Morrissette, N. S. and Bradley, P. J. (2010). A novel family of Toxoplasma IMC proteins displays a hierarchical organization and functions in coordinating parasite division. *PLoS Pathogens* **6**, e1001094.

Borchers, H. W. (2022). {pracma}: Practical Numerical Math Functions.

Bounkeua, V., Li, F. and Vinetz, J. M. (2010). In vitro generation of Plasmodium falciparum ookinetes. *The American journal of tropical medicine and hygiene* **83**, 1187-1194.

Bringmann, M., Landrein, B., Schudoma, C., Hamant, O., Hauser, M. T. and Persson, S. (2012). Cracking the elusive alignment hypothesis: the microtubule-cellulose synthase nexus unraveled. *Trends Plant Sci* **17**, 666-74.

Carey, K. L., Westwood, N. J., Mitchison, T. J. and Ward, G. E. (2004). A small-molecule approach to studying invasive mechanisms of Toxoplasma gondii. *Proc Natl Acad Sci U S A* **101**, 7433-8.

Carruthers, V. B., Sherman, G. D. and Sibley, L. D. (2000). The Toxoplasma adhesive protein MIC2 is proteolytically processed at multiple sites by two parasite-derived proteases. *The Journal of biological chemistry* **275**, 14346-53.

Carruthers, V. B. and Sibley, L. D. (1997). Sequential protein secretion from three distinct organelles of Toxoplasma gondii accompanies invasion of human fibroblasts. *Eur. J.Cell Biol.* **73**, 114-23.

Dag, O., Dolgun, A. and Konar, N. M. (2018). {onewaytests: An R Package for One-Way Tests in Independent Groups Designs}. *{The R Journal}* **10**, 175-199.

de Chaumont, F., Dallongeville, S., Chenouard, N., Hervé, N., Pop, S., Provoost, T., Meas-Yedid, V., Pankajakshan, P., Lecomte, T., Le Montagner, Y. et al. (2012). Icy: an open bioimage informatics platform for extended reproducible research. *Nat Methods* **9**, 690-6.

Del Rosario, M., Periz, J., Pavlou, G., Lyth, O., Latorre-Barragan, F., Das, S., Pall, G. S., Stortz, J. F., Lemgruber, L., Whitelaw, J. A. et al. (2019). Apicomplexan F-actin is required for efficient nuclear entry during host cell invasion. *EMBO Reports* **20**, e48896.

Dobrowolski, J. M., Carruthers, V. B. and Sibley, L. D. (1997). Participation of myosin in gliding motility and host cell invasion by Toxoplasma gondii. *Mol Microbiol* **26**, 163-73.

Dobrowolski, J. M. and Sibley, L. D. (1996). Toxoplasma invasion of mammalian cells is powered by the actin cytoskeleton of the parasite. *Cell* **84**, 933-9.

Donald, R. G. and Roos, D. S. (1994). Homologous recombination and gene replacement at the dihydrofolate reductase-thymidylate synthase locus in Toxoplasma gondii. *Molecular & Biochemical Parasitology* **63**, 243-53.

Dowle, M. and Srinivasan, A. (2022). data.table: Extension of 'data.frame'.

Dubey, J. P. (2008). The history of Toxoplasma gondii--the first 100 years. *The Journal of eukaryotic microbiology* **55**, 467-75.

Ershov, D., Phan, M.-S., Pylvänäinen, J. W., Rigaud, S. U., Le Blanc, L., Charles-Orszag, A., Conway, J. R. W., Laine, R. F., Roy, N. H., Bonazzi, D. et al. (2022). TrackMate 7: integrating state-of-the-art segmentation algorithms into tracking pipelines. *Nature Methods* **19**, 829-832.

Forster, B., Van De Ville, D., Berent, J., Sage, D. and Unser, M. (2004). Complex wavelets for extended depth ‐ of ‐ field: A new method for the fusion of multichannel microscopy images. *Microscopy research and technique* **65**, 33-42.

Fox, B. A., Ristuccia, J. G., Gigley, J. P. and Bzik, D. J. (2009). Efficient gene replacements in Toxoplasma gondii strains deficient for nonhomologous end joining. *Eukaryotic Cell* **8**, 520-9.

Frenal, K., Polonais, V., Marq, J. B., Stratmann, R., Limenitakis, J. and Soldati-Favre, D. (2010). Functional dissection of the apicomplexan glideosome molecular architecture. *Cell Host Microbe* **8**, 343-57.

Garnham, P. C., Bird, R. G. and Baker, J. R. (1962). Electron microscope studies of motile stages of malaria parasites. III. The ookinetes of Haemamoeba and Plasmodium. *Transactions of the Royal Society of Tropical Medicine and Hygiene* **56**, 116-20.

Gaskins, E., Gilk, S., DeVore, N., Mann, T., Ward, G. and Beckers, C. (2004). Identification of the membrane receptor of a class XIV myosin in Toxoplasma gondii. *The Journal of cell biology* **165**, 383-93.

Graindorge, A., Frenal, K., Jacot, D., Salamun, J., Marq, J. B. and Soldati-Favre, D. (2016). The Conoid Associated Motor MyoH Is Indispensable for Toxoplasma gondii Entry and Exit from Host Cells. *PLoS Pathogens* **12**, e1005388.

Gras, S., Jackson, A., Woods, S., Pall, G., Whitelaw, J., Leung, J. M., Ward, G. E., Roberts, C. W. and Meissner, M. (2017). Parasites lacking the micronemal protein MIC2 are deficient in surface attachment and host cell egress, but remain virulent in vivo. *Wellcome Open Res* **2**, 32.

Harding, C. R., Gow, M., Kang, J. H., Shortt, E., Manalis, S. R., Meissner, M. and Lourido, S. (2019). Alveolar proteins stabilize cortical microtubules in Toxoplasma gondii. *Nature communications* **10**, 401.

Harris, C. R., Millman, K. J., van der Walt, S. J., Gommers, R., Virtanen, P., Cournapeau, D., Wieser, E., Taylor, J., Berg, S., Smith, N. J. et al. (2020). Array programming with NumPy. *Nature* **585**, 357-362.

Heaslip, A. T., Nishi, M., Stein, B. and Hu, K. (2011). The motility of a human parasite, *Toxoplasma gondii*, is regulated by a novel lysine methyltransferase. *PLoS Pathog* **7**, e1002201.

Hopp, C. S., Chiou, K., Ragheb, D. R. T., Salman, A. M., Khan, S. M., Liu, A. J. and Sinnis, P. (2015). Longitudinal analysis of Plasmodium sporozoite motility in the dermis reveals component of blood vessel recognition. *Elife* **4**, e07789.

Hu, K. (2008). Organizational Changes of the Daughter Basal Complex during the Parasite Replication of *Toxoplasma gondii*. *PLoS Pathogens* **4**, 108-121.

Hu, K., Johnson, J., Florens, L., Fraunholz, M., Suravajjala, S., DiLullo, C., Yates, J., Roos, D. S. and Murray, J. M. (2006). Cytoskeletal components of an invasion machine – the apical complex of *Toxoplasma gondii*. *PLoS Pathogens* **2**, 0121-0139.

Hu, K., Roos, D. S. and Murray, J. M. (2002). A novel polymer of tubulin forms the conoid of Toxoplasma gondii. *The Journal of cell biology* **156**, 1039-50.

Huynh, M.-H. and Carruthers, V. B. (2006). Toxoplasma MIC2 is a major determinant of invasion and virulence. *PLoS Pathogens* **2**, e84.

Huynh, M. H. and Carruthers, V. B. (2009). Tagging of endogenous genes in a Toxoplasma gondii strain lacking Ku80. *Eukaryotic Cell* **8**, 530-9.

Huynh, M. H., Rabenau, K. E., Harper, J. M., Beatty, W. L., Sibley, L. D. and Carruthers, V. B. (2003). Rapid invasion of host cells by Toxoplasma requires secretion of the MIC2-M2AP adhesive protein complex. *The EMBO journal* **22**, 2082-90.

Jacot, D., Tosetti, N., Pires, I., Stock, J., Graindorge, A., Hung, Y. F., Han, H., Tewari, R., Kursula, I. and Soldati-Favre, D. (2016). An Apicomplexan Actin-Binding Protein Serves as a Connector and Lipid Sensor to Coordinate Motility and Invasion. *Cell Host & Microbe* **20**, 731-743.

Kan, A., Tan, Y.-H., Angrisano, F., Hanssen, E., Rogers, K. L., Whitehead, L., Mollard, V. P., Cozijnsen, A., Delves, M. J., Crawford, S. et al. (2014). Quantitative analysis of Plasmodium ookinete motion in three dimensions suggests a critical role for cell shape in the biomechanics of malaria parasite gliding motility. *Cellular Microbiology* **16**, 734-750.

Kassambara, A. (2023). {rstatix}: Pipe-Friendly Framework for Basic Statistical Tests.

Leung, J. M., He, Y., Zhang, F., Hwang, Y. C., Nagayasu, E., Liu, J., Murray, J. M. and Hu, K. (2017). Stability and function of a putative microtubule organizing center in the human parasite Toxoplasma gondii. *Molecular Biology of the Cell (Featured as Journal Cover)* **28**, 1361-1378.

Leung, J. M., Liu, J., Wetzel, L. A. and Hu, K. (2019). Centrin2 from the human parasite *Toxoplasma gondii* is required for its invasion and intracellular replication. *J Cell Sci*.

Leung, J. M., Rould, M. A., Konradt, C., Hunter, C. A. and Ward, G. E. (2014). Disruption of TgPHIL1 alters specific parameters of Toxoplasma gondii motility measured in a quantitative, three-dimensional live motility assay. *Plos One* **9**, e85763.

Liu, J., He, Y., Benmerzouga, I., Sullivan, W. J., Jr., Morrissette, N. S., Murray, J. M. and Hu, K. (2015). An ensemble of specifically targeted proteins stabilizes cortical microtubules in the human parasite Toxoplasma gondii. *Molecular Biology of the Cell (Featured as Journal Cover)* **27**, 549-71.

Liu, J., Wetzel, L., Zhang, Y., Nagayasu, E., Ems-McClung, S., Florens, L. and Hu, K. (2013). Novel Thioredoxin-Like Proteins Are Components of a Protein Complex Coating the Cortical Microtubules of *Toxoplasma gondii*. *Eukaryotic Cell* **12**, 1588-99.

Mehta, S. and Sibley, L. D. (2011). Actin depolymerizing factor controls actin turnover and gliding motility in Toxoplasma gondii. *Mol Biol Cell* **22**, 1290-9.

Meissner, M., Schluter, D. and Soldati, D. (2002). Role of Toxoplasma gondii myosin A in powering parasite gliding and host cell invasion. *Science* **298**, 837-40.

Mital, J., Meissner, M., Soldati, D. and Ward, G. E. (2005). Conditional expression of Toxoplasma gondii apical membrane antigen-1 (TgAMA1) demonstrates that TgAMA1 plays a critical role in host cell invasion. *Molecular Biology of the Cell* **16**, 4341-9.

Morrissette, N. S., Murray, J. M. and Roos, D. S. (1997). Subpellicular microtubules associate with an intramembranous particle lattice in the protozoan parasite Toxoplasma gondii. *J. Cell Sci.* **110**, 35-42.

Morrissette, N. S. and Sibley, L. D. (2002a). Cytoskeleton of apicomplexan parasites. *Microbiol Mol Biol Rev* **66**, 21-38.

Morrissette, N. S. and Sibley, L. D. (2002b). Disruption of microtubules uncouples budding and nuclear division in *Toxoplasma gondii*. *J Cell Sci* **115**, 1017-25.

Munera Lopez, J., Tengganu, I. F., Liu, J., Murray, J. M., Arias Padilla, L. F., Zhang, Y., Brown, P. T., Florens, L. and Hu, K. (2022). An apical protein, Pcr2, is required for persistent movement by the human parasite Toxoplasma gondii. *PLoS Pathog* **18**, e1010776.

Nagayasu, E., Hwang, Y.-c., Liu, J., Murray, J. and Hu, K. (2016). Loss of a doublecortin (DCX) domain containing protein causes structural defects in a tubulin-based organelle of *Toxoplasma gondii* and impairs host cell invasion. *Molecular Biology of the Cell* **E16-08-0587**

Nichols, B. A. and Chiappino, M. L. (1987). Cytoskeleton of Toxoplasma gondii. *J. Protozool.* **34**, 217-26.

Okuta, R., Unno, Y., Nishino, D., Hido, S. and Crissman. (2017). CuPy : A NumPy-Compatible Library for NVIDIA GPU Calculations.

Opitz, C. and Soldati, D. (2002). 'The glideosome': a dynamic complex powering gliding motion and host cell invasion by Toxoplasma gondii. *Mol Microbiol* **45**, 597-604.

Pavlou, G., Touquet, B., Vigetti, L., Renesto, P., Bougdour, A., Debarre, D., Balland, M. and Tardieux, I. (2020). Coupling Polar Adhesion with Traction, Spring, and Torque Forces Allows High-Speed Helical Migration of the Protozoan Parasite Toxoplasma. *ACS Nano* **14**, 7121-7139.

Periz, J., Whitelaw, J., Harding, C., Gras, S., Del Rosario Minina, M. I., Latorre-Barragan, F., Lemgruber, L., Reimer, M. A., Insall, R., Heaslip, A. et al. (2017). Toxoplasma gondii F-actin forms an extensive filamentous network required for material exchange and parasite maturation. *Elife* **6**, e24119.

Rabenau, K. E., Sohrabi, A., Tripathy, A., Reitter, C., Ajioka, J. W., Tomley, F. M. and Carruthers, V. B. (2001). TgM2AP participates in Toxoplasma gondii invasion of host cells and is tightly associated with the adhesive protein TgMIC2. *Mol Microbiol* **41**, 537-47.

Roos, D. S., Donald, R. G., Morrissette, N. S. and Moulton, A. L. (1994). Molecular tools for genetic dissection of the protozoan parasite *Toxoplasma gondii*. *Methods Cell Biol.* **45**, 27-78.

RStudioTeam. (2020). RStudio: Integrated Development for R. *RStudio, PBC, Boston, MA* **URL http://www.rstudio.com/**.

Sahoo, N., Beatty, W., Heuser, J., Sept, D. and Sibley, L. D. (2006). Unusual kinetic and structural properties control rapid assembly and turnover of actin in the parasite Toxoplasma gondii. *Molecular Biology of the Cell* **17**, 895-906.

Saxton, W. O. (1996). Semper: Distortion Compensation, Selective Averaging, 3-D Reconstruction, and Transfer Function Correction in a Highly Programmable System. *J Struct Biol* **116**, 230-6.

Schatten, H., Sibley, L. D. and Ris, H. (2003). Structural evidence for actin-like filaments in Toxoplasma gondii using high-resolution low-voltage field emission scanning electron microscopy. *Microsc Microanal* **9**, 330-5.

Schindelin, J., Arganda-Carreras, I., Frise, E., Kaynig, V., Longair, M., Pietzsch, T., Preibisch, S., Rueden, C., Saalfeld, S., Schmid, B. et al. (2012). Fiji: an open-source platform for biological-image analysis. *Nature Methods* **9**, 676-82.

Stadler, R. V., White, L. A., Hu, K., Helmke, B. P. and Guilford, W. H. (2017). Direct measurement of cortical force generation and polarization in a living parasite. *Mol Biol Cell* **E16-07-0518**.

Stokkermans, T. J., Schwartzman, J. D., Keenan, K., Morrissette, N. S., Tilney, L. G. and Roos, D. S. (1996). Inhibition of Toxoplasma gondii replication by dinitroaniline herbicides. *Exp. Parasitol.* **84**, 355-70.

Swedlow, J. R., Hu, K., Andrews, P. D., Roos, D. S. and Murray, J. M. (2002). Measuring tubulin content in Toxoplasma gondii: a comparison of laser-scanning confocal and wide-field fluorescence microscopy. *Proc Natl Acad Sci U S A* **99**, 2014-9.

Team, R. C. (2021). {R}: A Language and Environment for Statistical Computing. Vienna, Austria: R Foundation for Statistical Computing.

Tinevez, J. Y., Perry, N., Schindelin, J., Hoopes, G. M., Reynolds, G. D., Laplantine, E., Bednarek, S. Y., Shorte, S. L. and Eliceiri, K. W. (2017). TrackMate: An open and extensible platform for single-particle tracking. *Methods (San Diego, Calif)* **115**, 80-90.

Tosetti, N., Dos Santos Pacheco, N., Soldati-Favre, D. and Jacot, D. (2019). Three F-actin assembly centers regulate organelle inheritance, cell-cell communication and motility in Toxoplasma gondii. *Elife* **8**, e42669.

Tran, J. Q., Li, C., Chyan, A., Chung, L. and Morrissette, N. S. (2012). SPM1 stabilizes subpellicular microtubules in Toxoplasma gondii. *Eukaryot Cell* **11**, 206-16.

Van Rossum, G. a. D., Fred L. (2009). Python 3 Reference Manual. Scotts Valley, CA, USA: CreateSpace.

Wang, X., Qian, P., Cui, H., Yao, L. and Yuan, J. (2020). A protein palmitoylation cascade regulates microtubule cytoskeleton integrity in Plasmodium. *The EMBO journal* **39**, e104168-e104168.

Wetzel, D. M., Hakansson, S., Hu, K., Roos, D. and Sibley, L. D. (2003). Actin filament polymerization regulates gliding motility by apicomplexan parasites. *Mol Biol Cell* **14**, 396-406.

Wickham, H., Averick, M., Bryan, J., Chang, W., McGowan, L. D. A., François, R., Grolemund, G., Hayes, A., Henry, L., Hester, J. et al. (2019). Welcome to the {tidyverse}. *Journal of Open Source Software* **4**, 1686.

Wickham, H. and Seidel, D. (2022). {scales}: Scale Functions for Visualization.

World-Health-Organization. (2022). World Malaria Report 2022. 293.

Wortel, I. M. N., Liu, A. Y., Dannenberg, K., Berry, J. C., Miller, M. J. and Textor, J. (2021). CelltrackR: An R package for fast and flexible analysis of immune cell migration data. *ImmunoInformatics* **1-2**, 100003.

Xie, Y., Allaire, J. J. and Grolemund, G. (2018). R Markdown: The Definitive Guide. Boca Raton, Florida: Chapman and Hall/CRC.

Xie, Y., Dervieux, C. and Riederer, E. (2020). R Markdown Cookbook. Boca Raton, Florida: Chapman and Hall/CRC.

Figure 1

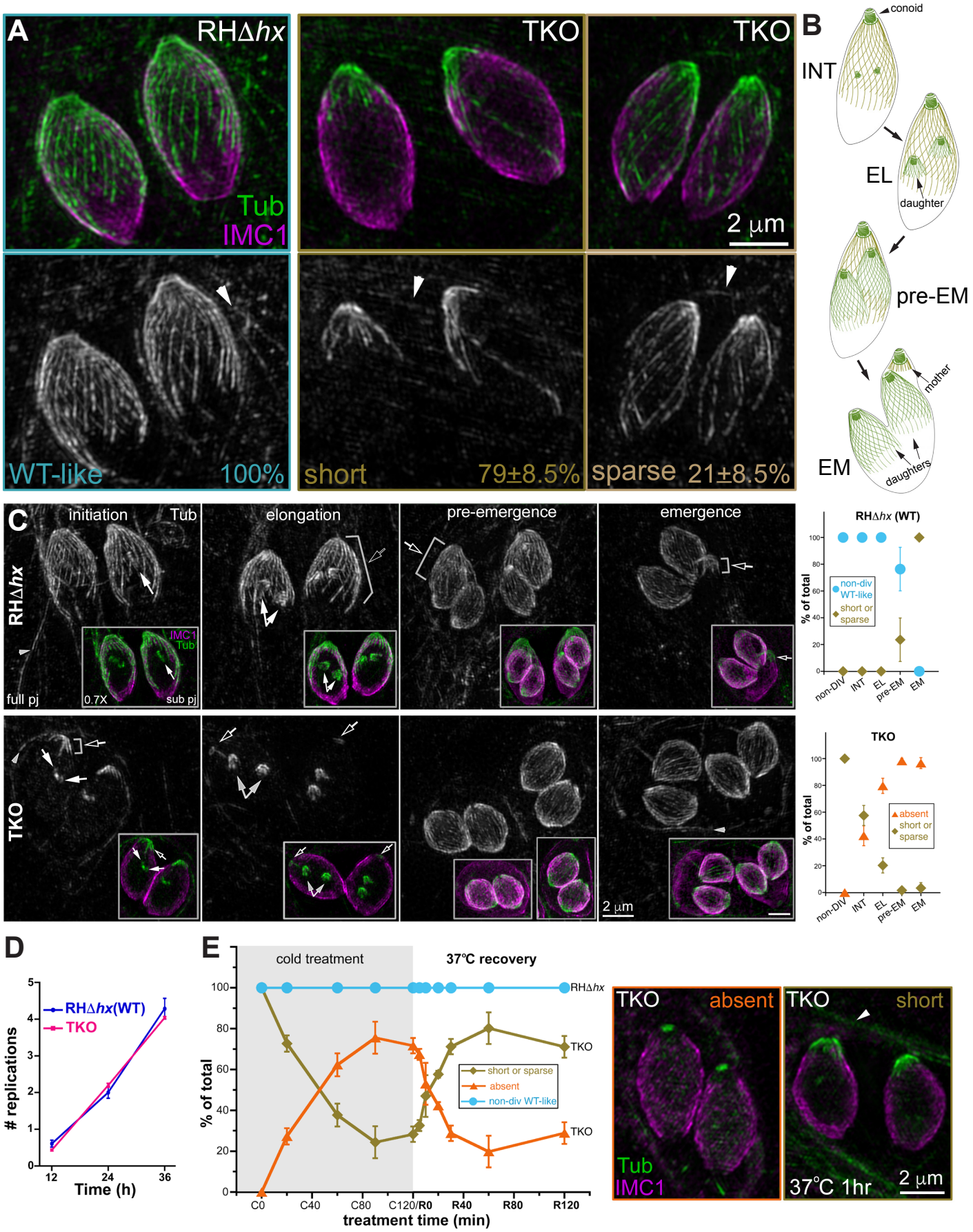
A
RHΔhx
TKO
TKO
Tub
IMC1
2 μm
WT-like
100%
short
79±8.5%
sparse
21±8.5%
B
conoid
INT
EL
daughter
pre-EM
mother
EM
daughters
C
initiation
Tub
elongation
pre-emergence
emergence
RHΔhx
IMC1
Tub
full pj
0.7X
sub pj
TKO
2 μm
RHΔhx (WT)
% of total
non-div WT-like
short or sparse
non-DIV
INT
EL
pre-EM
EM
TKO
absent
short or sparse
D
RHΔhx(WT)
TKO
replications
Time (h)
E
cold treatment
37°C recovery
RHΔhx
TKO
TKO
short or sparse
absent
non-div WT-like
% of total
C0
C40
C80
C120/R0
R40
R80
R120
treatment time (min)
TKO
absent
Tub
IMC1
TKO
short
37°C 1hr
2 μm

Figure 2

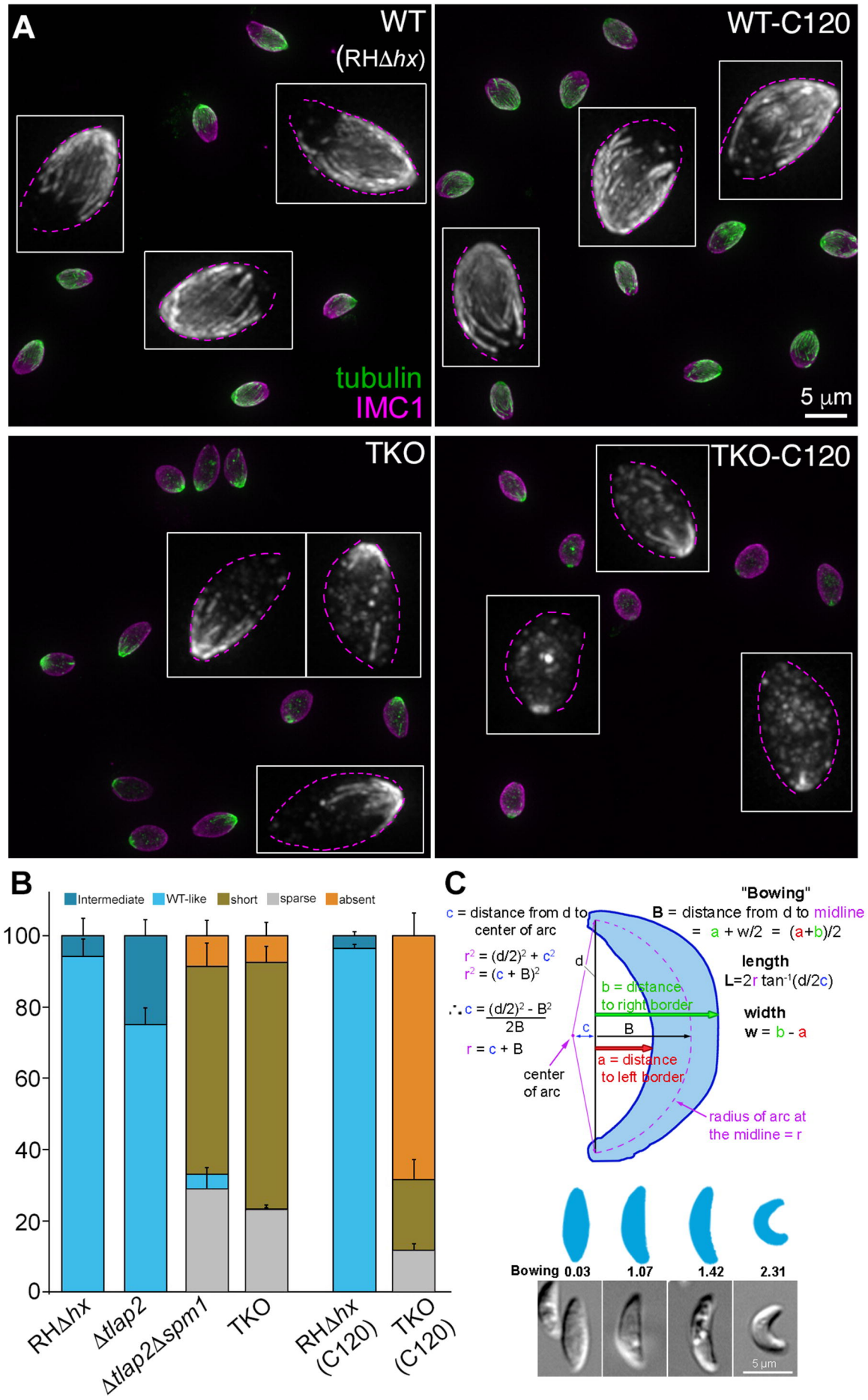
A
WT
(RHΔhx)
WT-C120
tubulin
IMC1
5 μm
TKO
TKO-C120
B
Intermediate
WT-like
short
sparse
absent
100
80
60
40
20
0
RHΔhx
Δtlap2
Δtlap2Δspm1
TKO
RHΔhx (C120)
TKO (C120)
C
"Bowing"
c = distance from d to center of arc
B = distance from d to midline = a + w/2 = (a+b)/2
r² = (d/2)² + c²
r² = (c + B)²
∴ c = ((d/2)² - B²)/2B
r = c + B
length
L=2r tan⁻¹(d/2c)
width
w = b - a
d
b = distance to right border
c
B
a = distance to left border
center of arc
radius of arc at the midline = r
Bowing 0.03
1.07
1.42
2.31
5 μm

Figure 3

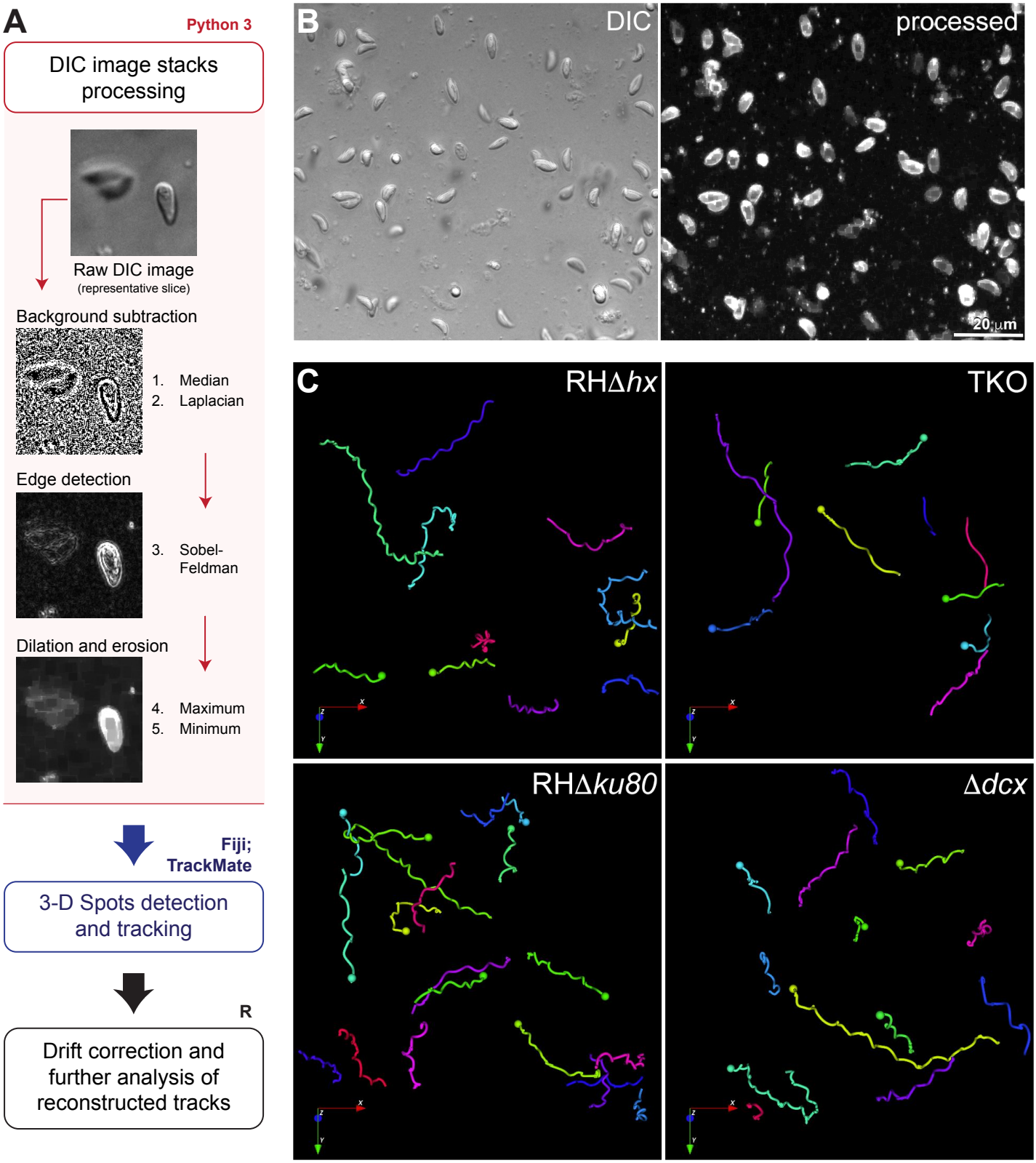
A
Python 3
DIC image stacks processing
Raw DIC image
(representative slice)
Background subtraction
1. Median
2. Laplacian
Edge detection
3. Sobel-Feldman
Dilation and erosion
4. Maximum
5. Minimum
Fiji; TrackMate
3-D Spots detection and tracking
R
Drift correction and further analysis of reconstructed tracks
B
DIC
processed
20 µm
C
RHΔhx
TKO
RHΔku80
Δdcx

Figure 4

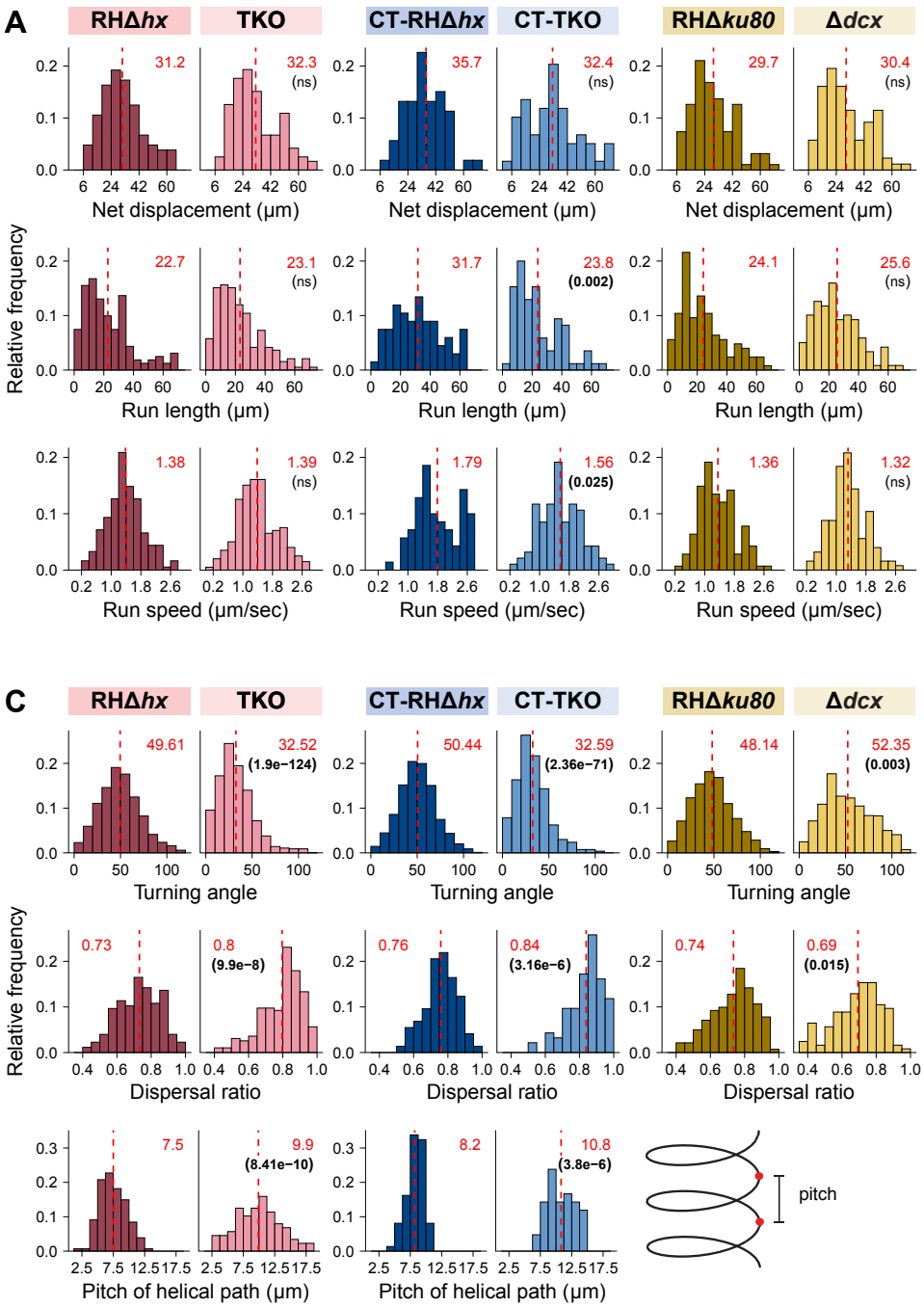
A
RHΔhx
TKO
CT-RHΔhx
CT-TKO
RHΔku80
Δdcx
31.2
32.3 (ns)
35.7
32.4 (ns)
29.7
30.4 (ns)
Net displacement (μm)
Relative frequency
22.7
23.1 (ns)
31.7
23.8 (0.002)
24.1
25.6 (ns)
Run length (μm)
1.38
1.39 (ns)
1.79
1.56 (0.025)
1.36
1.32 (ns)
Run speed (μm/sec)
C
49.61
32.52 (1.9e−124)
50.44
32.59 (2.36e−71)
48.14
52.35 (0.003)
Turning angle
0.73
0.8 (9.9e−8)
0.76
0.84 (3.16e−6)
0.74
0.69 (0.015)
Dispersal ratio
7.5
9.9 (8.41e−10)
8.2
10.8 (3.8e−6)
Pitch of helical path (μm)
pitch

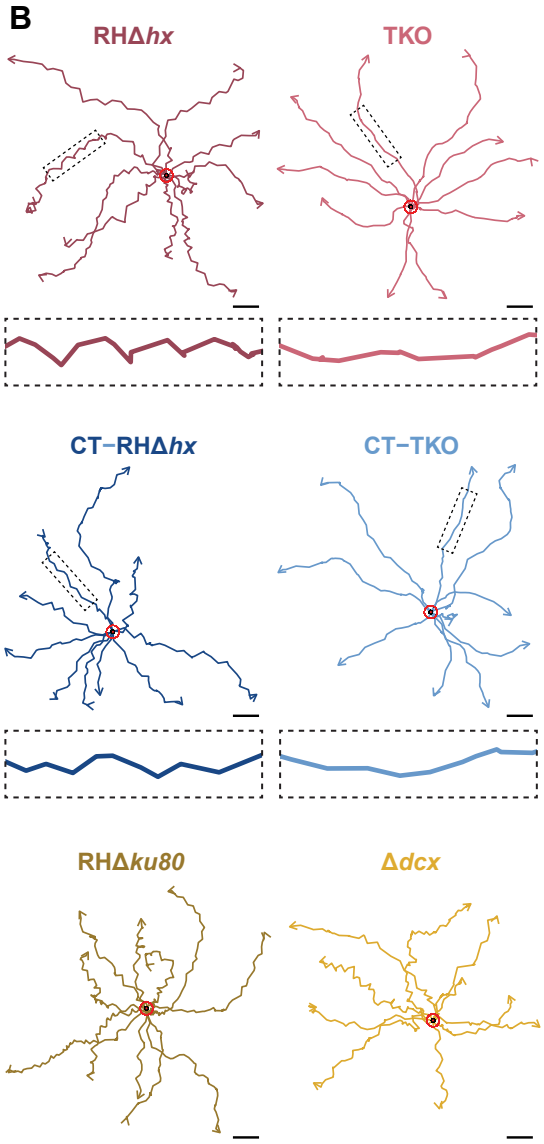
B
RHΔhx
TKO
CT−RHΔhx
CT−TKO
RHΔku80
Δdcx

Figure 5

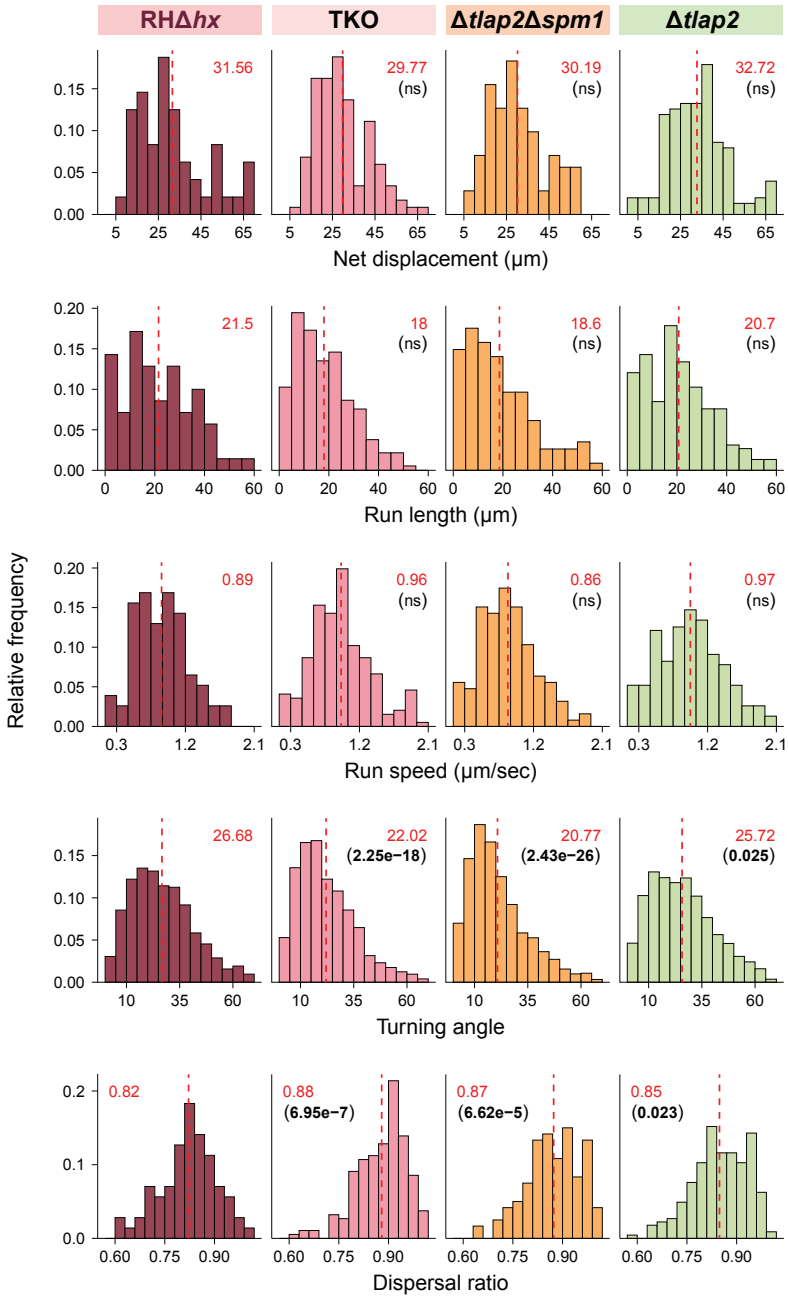
RHΔhx
TKO
Δtlap2Δspm1
Δtlap2
31.56
29.77
(ns)
30.19
(ns)
32.72
(ns)
Net displacement (μm)
21.5
18
(ns)
18.6
(ns)
20.7
(ns)
Run length (μm)
Relative frequency
0.89
0.96
(ns)
0.86
(ns)
0.97
(ns)
Run speed (μm/sec)
26.68
22.02
(2.25e−18)
20.77
(2.43e−26)
25.72
(0.025)
Turning angle
0.82
0.88
(6.95e−7)
0.87
(6.62e−5)
0.85
(0.023)
Dispersal ratio

Figure 6

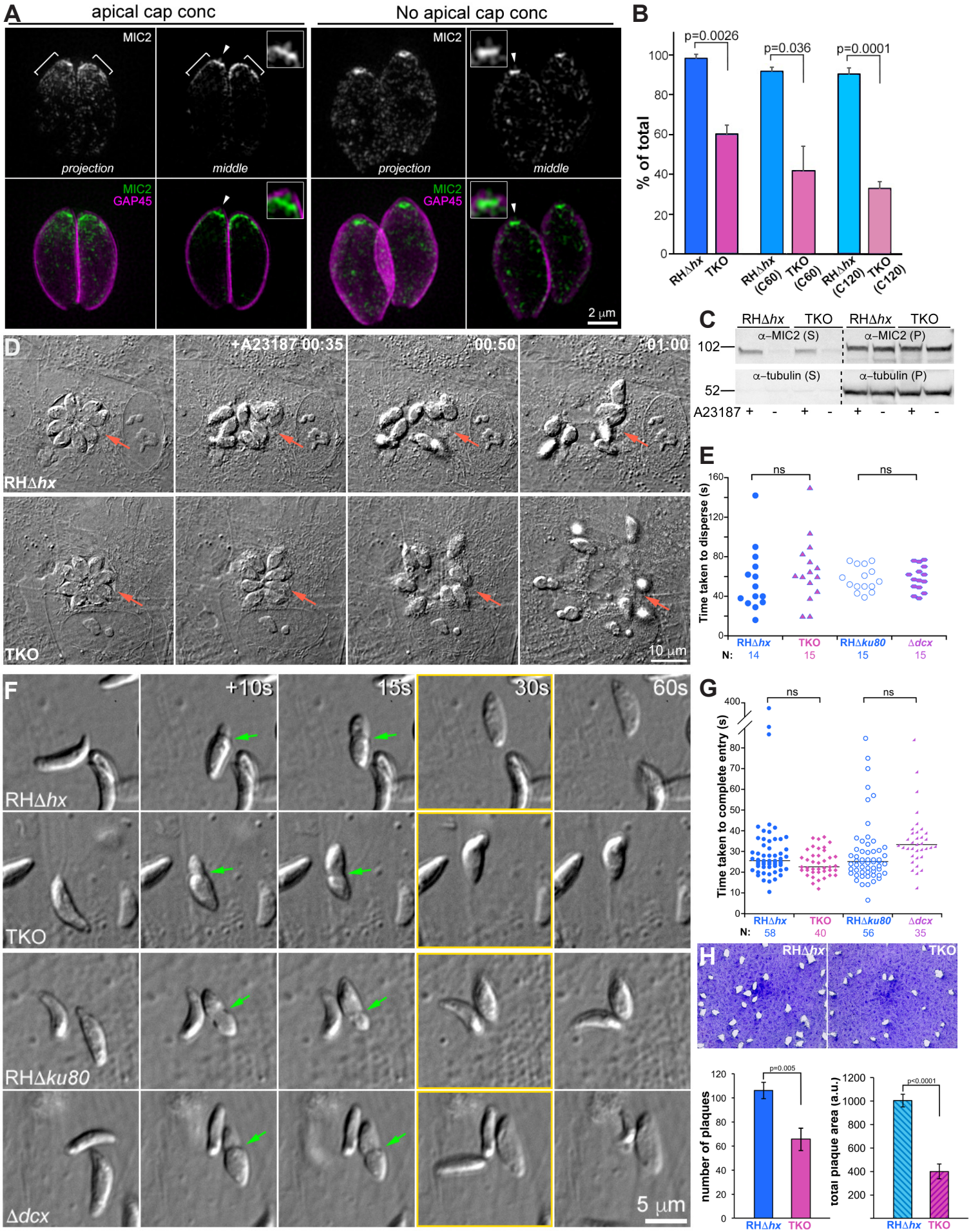
A
apical cap conc
No apical cap conc
MIC2
projection
middle
MIC2
GAP45
2 µm
B
p=0.0026
p=0.036
p=0.0001
% of total
RHΔhx
TKO
RHΔhx (C60)
TKO (C60)
RHΔhx (C120)
TKO (C120)
C
RHΔhx
TKO
α–MIC2 (S)
α–MIC2 (P)
α–tubulin (S)
α–tubulin (P)
102
52
A23187
D
+A23187 00:35
00:50
01:00
RHΔhx
TKO
10 µm
E
ns
Time taken to disperse (s)
RHΔhx
TKO
RHΔku80
Δdcx
N:
14
15
15
15
F
+10s
15s
30s
60s
RHΔhx
TKO
RHΔku80
Δdcx
5 µm
G
ns
Time taken to complete entry (s)
RHΔhx
TKO
RHΔku80
Δdcx
N:
58
40
56
35
H
RHΔhx
TKO
p=0.005
number of plaques
p<0.0001
total plaque area (a.u.)
RHΔhx
TKO

Supplemental Videos and Figures:

Video S1: Time-lapse microscopy of 3-D motility in 50% Matrigel for the RH*Δhx* (RH parental 1) and TKO parasites. *Left:* Videos of projected DIC images (projections of 3-D stack generated by Stack focuser in ImageJ/Fiji). *Right:* Corresponding processed images with a subset of 3-D trajectories. Time interval: ~ 1.36 sec. Video speed: 10 frames/s.

Video S2: Rotational view of 3-D trajectories for the RH*Δhx* (RH parental 1) and TKO parasites included in Video S1. The traveling sphere associated with each track represents the centroid of the parasite traveling along that path. Length of arrow= 16 μm

Video S3: Time-lapse microscopy of 3-D motility in 50% Matrigel for the RH*Δku80* (RH parental 2) and *Δdcx* (*dcx KO*) parasites. *Left:* Videos of projected DIC images (projections of 3-D stack generated by Stack focuser in ImageJ/Fiji). *Right:* Corresponding processed images with a subset of 3-D trajectories. Time interval: ~ 1.36 sec. Video speed: 10 frames/s.

Video S4: Rotational view of 3-D trajectories for the RH*Δku80* (RH parental 2) and *Δdcx* (*dcx KO*) parasites included in Video S3. The traveling sphere associated with each track represents the centroid of the parasite traveling along that path. Length of arrow= 16 μm

Video S5: Time-lapse microscopy of A23187 induced-egress for RH*Δhx* (RH parental) and TKO parasites. A23187 was added at the beginning of the movies to a final concentration of 5 μM. The intracellular wild-type and TKO parasite cultures were placed at 7°C for 1 hr prior to the egress experiment, which was conducted at 37°C. Time interval: 1 sec. Video speed: 60 frames/s. Scale bar: 5 μm.

Video S6: Time-lapse microscopy of host cell entry for RH*Δhx* (RH parental 1), TKO and RH*Δku80* (RH parental 2) and *Δdcx* (*dcx KO*) parasites. Fig 6F includes images selected from the timelapses in the leftmost column. Time interval: 1 sec. Video speed: 6 frames/s. Scale bar: 5 μm.

Figure S1 (Blot Transparency)
Top: Image of Western blot that contains data displayed in Fig 6C. Western blot of the secreted (supernatant) and unsecreted (pellet) fractions of RH*Δhx* and TKO parasites with (+) or without (-) A23187 treatment. The blot was probed by antibodies against MIC2 and tubulin. Lanes for molecular weight ladders are included.
Bottom: Quantification of levels of MIC2 in the secreted fractions upon A23187 stimulation in the RH*Δhx* parental and TKO parasites in 3 independent biological replicates.

Figure S2. Full and subset projections of 3D-SIM image stacks of dividing intracellular *mEmeraldFP-TLAP2* knock-in parasites showing that TLAP2 is recruited to the daughter cortical microtubules. Green and grayscale: mEmerald-FP-TLAP2. Magenta: apical cortex labeling with a mouse anti-ISP1 antibody. Parasites at an earlier (top) and a later stage (bottom) of daughter formation are shown.

Figure S1 (Blot Transparency)

Quantification of levels of MIC2 in the secreted fractions upon A23187 stimulation in the RHΔhx parental and TKO parasites in 3 independent biological replicates. For each sample, the MIC2 secretion is normalized against tubulin in the pellet from the same sample.

Parasite strain	replicate 1	replicate 2	replicate 3	average ± *SEM*
RHΔ*hx*	0.30	0.44	0.68	0.48±0.14
TKO	0.21	0.31	0.42	0.31±0.07

Figure S2

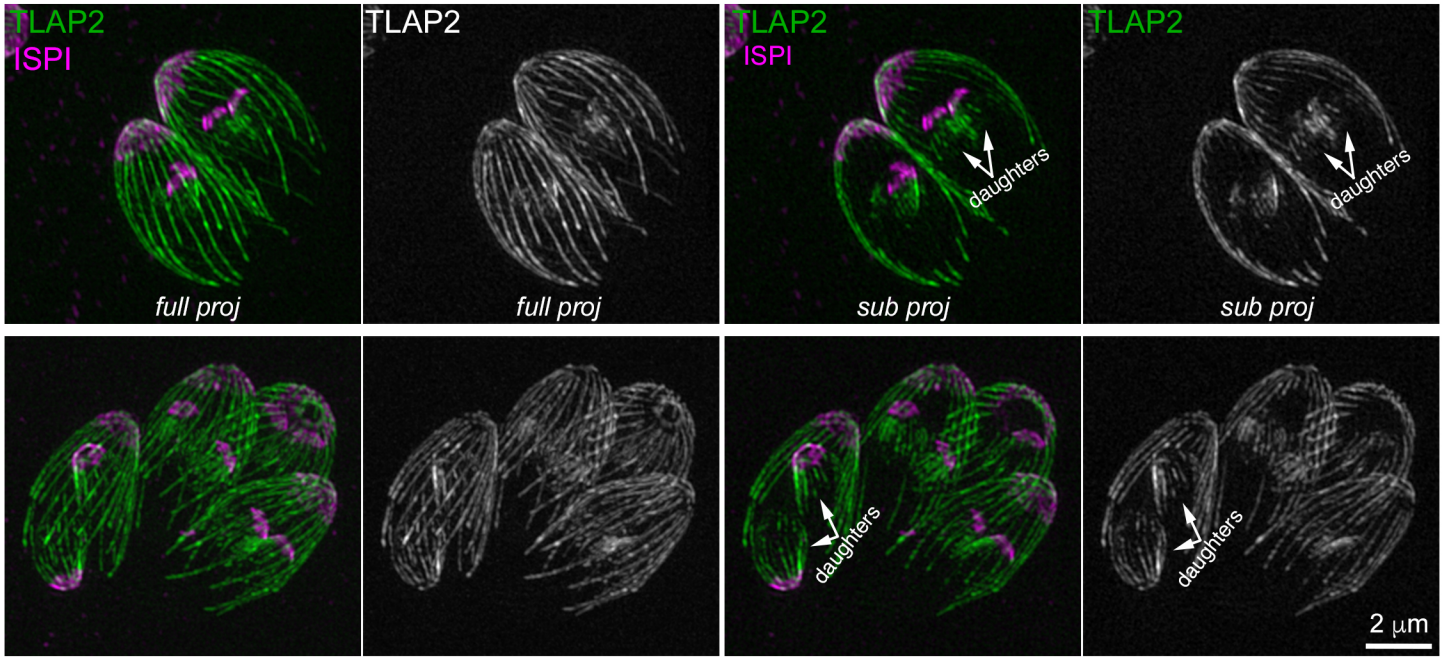
TLAP2
ISPI
full proj
TLAP2
full proj
TLAP2
ISPI
daughters
sub proj
TLAP2
daughters
sub proj
daughters
daughters
2 μm